Applied Food Research 6 (2026) 102480

Contents lists available at ScienceDirect

Applied Food Research

journal homepage: www.elsevier.com/locate/afres

# Amino-functionalized MIL-53(Al)@ PLA indicator for real-time colorimetric detection in intelligent fish packaging

Razieh Mansouri Habibabadi [a], Kazem Karami [a,*], Zahra Teymouri [b], Hajar Shekarchizadeh [b]

[a] Department of Chemistry, Isfahan University of Technology, Isfahan, 84156-83111, Iran
[b] Department of Food Science and Technology, College of Agriculture, Isfahan University of Technology, Isfahan, 84156-83111, Iran

ARTICLE INFO

*Keywords:*
Colorimetric indicator
Fish quality
Metal–organic framework
Food safety

ABSTRACT

Ensuring the freshness and safety of perishable foods requires intelligent indicators capable of real-time spoilage monitoring. In this study, a high-performance colorimetric indicator was developed by incorporating an amino-functionalized aluminum-based metal-organic framework, $NH_2$−MIL-53(Al), into a poly(lactic acid) (PLA) matrix. The composite film ($NH_2$−MIL-53(Al)@PLA) exhibited uniform particle dispersion and improved thermal stability up to approximately 450 °C, alongside a 2.5% reduction in moisture absorption compared to neat PLA. While the tensile strength and elongation at break decreased from 40.58 to 13.36 MPa and 27.25% to 1.12%, respectively, the film demonstrated significant antibacterial activity via a modified well assay against *Escherichia coli* and *Staphylococcus aureus*, yielding clear inhibition zones of 21.20 ± 0.10 and 30.34 ± 0.22 mm, respectively. Notably, the indicator showed a rapid and irreversible colorimetric response to volatile amines, achieving a low limit of detection (LOD) of 5.24 μM (gas-phase equivalent of 128.12 ppm) and a limit of quantification (LOQ) of 15.90 μM. ICP-OES migration studies confirmed high food safety, with negligible aluminum release in water (<0.02 mg $kg^{-1}$) and 10% ethanol (<0.20 mg $kg^{-1}$), remaining well below specific migration limits. Furthermore, the color transition from creamy white to dark brown accurately correlated with matrix pH, total volatile basic nitrogen (TVB-N), and total viable count (TVC), displaying high determination coefficients ($R^2$ = 0.981–0.998). These quantitative findings demonstrate that the developed composite film is a safe, stable, and highly sensitive tool for the visual monitoring of fish spoilage.

## 1. Introduction

Food safety has become a major public health concern, receiving increasing attention as awareness of food safety grows. Meat products such as pork, fish, and shrimp, which are rich in protein and fat, play an important role in the human diet. However, these protein-rich foods are prone to spoilage due to bacterial contamination, leading to the gradual release of volatile basic compounds such as ammonia and alkylamines (Xu et al., 2025). Among these compounds, ammonia, characterized by its strong and distinctive odor, is widely used as a key indicator for evaluating food freshness (Wang, 2024). The presence of ammonia not only impairs food quality by creating an unpleasant odor and taste but also poses potential health risks, including dizziness, nausea, and adverse effects on the digestive system (Zhang et al., 2025). Therefore, rapid and accurate detection of freshness is essential to help consumers make informed choices regarding food quality.

The total volatile basic nitrogen (TVB-N) assay remains the standard for evaluating meat freshness; however, its complex preparation, lengthy analysis, and high cost hinder on-site application. This limitation highlights the need for rapid, accurate, and non-destructive methods for the real-time meat quality assessment. Although analytical techniques such as liquid chromatography, electrochemical and optical sensors, and conductive polymers effectively detect spoilage compounds, they are often expensive, labor-intensive, and unsuitable for routine use (Kang et al., 2024). Consequently, there is an increasing demand for simple, low-cost, and rapid approaches for non-destructive monitoring of aquatic and meat products. Therefore, intelligent labels have emerged as a promising solution, enabling real-time detection and continuous monitoring of food freshness. Modern intelligent packaging integrates biosensors, humidity and time–temperature indicators, and particularly pH-responsive systems based on natural plant extracts, which have become a major focus in intelligent food packaging research (Poddar et al., 2025).

Among various polymeric matrices used in intelligent packaging,

* Corresponding author.
*E-mail address:* karami@iut.ac.ir (K. Karami).

https://doi.org/10.1016/j.afres.2026.102480
Received 4 February 2026; Received in revised form 15 July 2026; Accepted 4 August 2026
Available online 5 August 2026

polylactic acid (PLA), a biodegradable aliphatic polyester derived from renewable sources such as corn starch and sugarcane, is widely favored for its excellent film-forming ability, tensile strength, and optical clarity (Wu et al., 2022). For example, Akbari and Nikoo (2025) developed a pH-responsive PLA/polyethylene glycol (PEG) film containing elderberry anthocyanins for chicken spoilage monitoring. The film exhibited distinct color transitions from pink or purple to brown or grey in response to pH and ammonia vapors, providing sensitive, real-time freshness indication over six days of refrigerated storage (Akbari & Nikoo, 2025). Similarly, Ghorbani et al. (2021) fabricated a halochromic PLA-based film incorporating PEG, calcium bentonite, and *Malva sylvestris* anthocyanins to evaluate the freshness of minced meat, chicken, shrimp, and fish roe. This indicator showed a broad color range from light red at pH 2 to green at pH 11 and a strong correlation with TVB-N values, effectively distinguishing fresh, moderately fresh, and spoiled samples (Ghorbani et al., 2021).

Despite their promising performance, PLA–anthocyanin films face challenges such as pigment instability under light, temperature, and pH variations, as well as complex and costly extraction processes. Their sensing function is mainly limited to pH variation, which restricts the long-term stability and scalability of PLA-based intelligent packaging systems (Prakash et al., 2025).

Metal-organic frameworks (MOFs), crystalline porous materials composed of metal ions and organic ligands, offer high surface area, tunable porosity, and excellent chemical stability, making them robust freshness indicators with superior sensitivity and durability compared to natural pigments (Kang et al., 2024). For instance, Huang et al. (2024) incorporated roselle anthocyanins and various MOFs into polyvinyl alcohol/corn starch films, where the aluminum-based $NH_2$-MIL-101(Al) exhibited outstanding pH responsiveness and stability, showing a distinct red-to-blue transition during pork freshness monitoring. This performance was attributed to strong coordination between $Al^{3+}$ centers and anthocyanins, which minimized pigment migration and enhanced film integrity (Huang et al., 2025). However, hybrid pigment–MOF systems are limited because their colorimetric response mainly relies on the protonation–deprotonation of natural dyes, while the MOF serves only as a stabilizing matrix, making them susceptible to photodegradation, moisture, and poor signal reproducibility. In contrast, pure MOF-based indicators utilize intrinsic metal–ligand charge transfer, redox, or luminescence transitions, providing higher structural stability, more reversible optical responses, and greater resistance to environmental stress (Kang et al., 2024; Huang et al., 2025). Therefore, MOFs alone constitute a chemically stable and tunable platform for precise, real-time colorimetric freshness detection.

In this study, $NH_2$-MIL-53(Al), a highly porous metal–organic framework with tunable surface reactivity, was immobilized onto a biodegradable polylactic acid matrix to form a novel $NH_2$-MIL-53(Al) @PLA composite colorimetric indicator. The open $Al^{3+}$ sites and amino functionalities of $NH_2$-MIL-53(Al) synergistically and selectively interact with volatile amines released during fish spoilage. This interaction occurs via coordinative binding to unsaturated aluminum centers and hydrogen bonding with the $–NH_2$ groups of the framework, inducing strong and irreversible colorimetric changes through perturbation of the electronic structure of the MOF.

The PLA matrix ensures mechanical stability and environmental compatibility while allowing diffusion of spoilage-related compounds to the MOF sites. These features underscore the potential of MOF–PLA composites as next-generation intelligent packaging materials capable of providing chemically robust, non-destructive, real-time seafood freshness detection.

## 2. Materials and methods

### 2.1. Materials

Fresh trout fillet was purchased locally (Isfahan, Iran). Polylactic acid (PLA) granules (density: 1.25 ± 0.02 g/mL; molecular weight: 1.42 × $10^4$ Da) were purchased from Khatam Polymer Co. (Tehran, Iran). 2-aminoterephthalic acid ($NH_2$-BDC, 99%), N,N-dimethylformamide (DMF), methanol ($CH_3OH$), acetone ($C_3H_6O$), aluminum chloride ($AlCl_3$), deionized water, trimethylamine ($C_3H_9N$), acetic acid ($C_2H_4O_2$, 99%), chloroform ($CHCl_3$, 99%), ethanol ($C_2H_5OH$), sodium chloride (NaCl), ammonia solution ($NH_4OH$, 25%), plate count agar (PCA), and nutrient agar (NA) were purchased from Merck KGaA Co., Ltd. (Darmstadt, Germany).

### 2.2. $NH_2$-MIL-53(Al) synthesis and characterization

$NH_2$-MIL-53(Al) was fabricated following Habibabadi et al. (2026). First, 3 mmol of $NH_2$-BDC was dissolved in 20 mL of deionized water to prepare solution A. Separately, 3 mmol of $AlCl_3$ was dissolved in 10 mL of deionized water to create solution B. Solution A was stirred with a magnetic stirrer while solution B was slowly adding dropwise under continuous stirring. The mixture was stirred for an hour. Then, this combined solution was transferred to a steel autoclave with Teflon container and heated in a conventional oven at 150 °C for 5 h. After cooling to room temperature, the product was collected by centrifugation and washed three times with deionized water. To eliminate any unreacted materials and open the pores, the precipitate was stirred in 20 mL of DMF for 24 h. Following centrifugation to remove the solvent, the product was suspended in 20 mL methanol and stirred for 72 h. Finally, the precipitate was dried under vacuum at 70 C for 24 h and then calcined in a conventional oven at 200 °C for 4 h (Rahimpoor et al., 2022). The morphology and particle size of $NH_2$−MIL-53(Al) were examined by field emission scanning electron microscopy (FE-SEM)) QUANTA FEG450, USA). The particle size distribution was further evaluated using ImageJ software. Nitrogen adsorption–desorption isotherms were measured to determine the specific surface areas and pore size distribution using the Brunauer–Emmett–Teller (BET) method with a BELSORP Mini II surface area analyzer (Japan). To evaluate the colorimetric response of $NH_2$-MIL-53(Al) toward ammonia, 0.1 g of the MOF powder was placed inside a sealed chamber containing volatile ammonia released from a 100 μM aqueous ammonia solution. After 60 s of headspace exposure at room temperature, photographs of the samples were recorded under identical illumination conditions using a smartphone camera (Redmi Note 13, Xiaomi, China; 200 MP main camera) to visually assess the color transition. Additionally, the absorbance spectra of $NH_2$-MIL-53(Al) solutions were recorded by spectrophotometry (JASCO V-570) over the wavelength range of 200 to 700 nm following exposure to varying concentrations of ammonia (0, 25, 50, 60, and 70 μM).

### 2.3. Synthesis of colorimetric indicator based on PLA matrix containing $NH_2$-MIL-53(Al)

The colorimetric indicator was fabricated following a modified procedure based on the method reported by González and Igartzabal, using PLA through the solvent casting technique (Teymouri et al., 2025). In detail, 2 g of PLA granules were dissolved in 100 mL of chloroform under continuous stirring for 8 h. Separately, to improve particle dispersion, 2 wt% of $NH_2$-MIL-53(Al) was prepared by suspending the requisite amount of MOF powder in distilled water and subjecting it to ultrasonic treatment for 10 min using an ultrasonic bath (LABORETTE, 35 kHz, Germany). This fresh suspension was then added dropwise to the PLA solution after its initial 2 h of dissolution, and stirring was maintained for the remaining 6 h. Subsequently, 40 mL of the homogeneous mixture was carefully poured into a glass Petri dish and left to dry at room temperature (25 C) for 4 h to form the indicator. Prior to characterization and performance testing, all prepared indicator films were conditioned in a desiccator at 25± 2 °C and 76% relative humidity (RH) for at least 48 h to ensure environmental equilibrium and comparability of results.

### 2.4. Characterization of $NH_2$-MIL-53(Al)@PLA colorimetric indicator

#### 2.4.1. Structural, chemical, and thermal characterization

FE-SEM analysis was employed to examine the morphology of the $NH_2$-MIL-53(Al)@PLA indicator. The Fourier transform infrared spectra in attenuated total reflectance mode (FTIR-ATR) were obtained using a Tensor 27 spectrometer (Bruker, Germany) within the wavenumber range of 600–4000 $cm^{-1}$. Powder X-ray diffraction (PXRD) patterns were recorded using an X-ray diffractometer (AW-XDM300, ASENWARE, China) equipped with Cu Kα radiation (λ = 1.54184 Å, 40 kV, 30 mA) spanning a 2θ range of 5–70°. The thermal stability of pristine $NH_2$-MIL-53(Al) and the $NH_2$-MIL-53(Al)@PLA indicator was evaluated using a simultaneous thermal analyzer (STA 449 F3 Jupiter, NETZSCH, Germany). Samples were heated from 25 to 800 °C at a heating rate of 20 °C $min^{-1}$ under a nitrogen atmosphere (50 mL $min^{-1}$).

#### 2.4.2. Thickness and mechanical properties

Film thickness was measured using a conventional micrometer (Mitutoyo-Co, Tokyo, Japan) with an accuracy of 0.001 mm. Measurements were taken at three random positions on each indicator film, and the average values were calculated (Wang et al., 2023).

The mechanical performance of neat PLA and $NH_2$-MIL-53(Al)@PLA indicators was assessed in terms of tensile strength (TS) and elongation at break (EB) using a Universal Testing Machine (Bongshin DBBP 20, Busan, South Korea). The measurements were performed at 25 °C with a crosshead speed of 50 mm $min^{-1}$ and an initial gauge length of 45 mm. The maximum load capacity of the load cell was 20 kN. The TS and EB values were determined according to Eqs. (1) and (2), respectively (Amaregouda et al., 2022)

$$\text{Tensile strength (MPa)} = \frac{F_{max}(N)}{A(m^2)} \quad (1)$$

$$\text{Elongation at break (\%)} = \frac{L_{max}(m)}{L(m)} \times 100 \quad (2)$$

where $F_{max}$ represents the maximum force applied (N), A is the initial cross-sectional area of the film ($m^2$), $L_{max}$ represent the indicators length at the breaking point (m), and $L_0$ corresponds to the initial film length prior to testing (m).

#### 2.4.3. Sensitivity to pH changes

The colorimetric response of the $NH_2$-MIL-53(Al)@PLA indicator was evaluated over a pH range of 5 to 11 by immersing the indicator in Britton-Robinson buffer solutions. The colorimetric parameters (L*, a*, and b*) were then measured using a colorimeter (Nippon Denshoku ZE6000, Japan). The total color difference (ΔE) was calculated according to Eq. (3)

$$\Delta E = \sqrt{\left(L_0^* - L^*\right)^2 + \left(a_0^* - a^*\right)^2 + \left(b_0^* - b^*\right)^2} \quad (3)$$

where, $L_0$*, $a_0$*, and $b_0$* denote the color parameters of the initial indicator, while L*, a*, and b* correspond to the color parameters of the indicator after exposure to different pH levels (Teymouri et al., 2025).

#### 2.4.4. Ammonia sensitivity

The colorimetric sensitivity of the $NH_2$–MIL-53(Al)@PLA indicator toward ammonia was evaluated using sealed glass vials (15 mL) containing 10 mL of ammonia solutions at different concentrations (0–100 μM). Circular indicator films (2 cm in diameter) were fixed to the inner side of the vial caps, and the vials were immediately sealed to expose the films to the generated headspace vapor at a controlled temperature of 25 °C. After 60 s of exposure, the colorimetric response of the indicators was determined by measuring the color parameters (L*, a*, and b*) using a colorimeter, and the total color difference (ΔE) was calculated according to Eq. (3). Concurrently, digital images were recorded under identical illumination using a smartphone camera (Redmi Note 13, Xiaomi, China; 200 MP main camera) to visually document the naked-eye color transitions. The limit of detection (LOD) and limit of quantification (LOQ) were calculated from the calibration curves according to Eqs. (4) and 5, respectively (Teymouri et al., 2025). To facilitate benchmarking against gas-phase packaging thresholds, the liquid-phase detection threshold was converted into its upper-bound theoretical gas-phase equivalent (ppm v/v) using the ideal gas relationship (PV = nRT) under standard conditions, assuming a comprehensive worst-case scenario of complete analyte volatilization into the headspace (Lentz et al., 2019).

$$\text{LOD} = \frac{3.3\sigma}{S} \quad (4)$$

$$\text{LOQ} = \frac{10\sigma}{S} \quad (5)$$

where, σ denotes the standard deviation calculated from eight replicates, while S represents the slope of the calibration curve.

Furthermore, the colorimetric response of the $NH_2$-MIL-53(Al)@PLA indicator toward ammonia was evaluated to determine its sensitivity. For this purpose, indicator samples (18 × 18 $mm^2$) were exposed to the headspace of a 10 mL ammonia solution (20 μM) for 120 min. The resulting color variations were recorded, and the corresponding ΔE values were determined according to Eq. (3) (Zhang et al., 2024).

#### 2.4.5. Selectivity

Selectivity is a crucial feature for the reliable operation of colorimetric indicator, especially in situations like intelligent packaging, where the indicator may be exposed to multiple volatile compounds. An optimal indicator should distinctly recognize specific target analytes, such as nitrogen-containing volatile compounds, without interference from other non-target volatiles. The selective responsiveness of the $NH_2$-MIL-53(Al)@PLA indicator to ammonia gas was investigated. For this purpose, the $NH_2$-MIL-53(Al)@PLA indicator was placed inside the lid of a glass vial containing 100 μM concentrations of various volatile compounds, including ethanol, acetone, trimethylamine, and acetic acid. The variations in the colorimetric parameters of the indicator were measured using a colorimeter to evaluate its selectivity (Zhai et al., 2019).

#### 2.4.6. Moisture absorption

To evaluate the moisture absorption capacity, $NH_2$-MIL-53(Al)@PLA indicator films were placed in a desiccator containing distilled water at 25 °C. The initial weight of each film ($w_o$) was recorded, and the samples were weighed daily for 9 days ($w_t$). The percentage of moisture absorption for both the control (PLA) and the $NH_2$-MIL-53(Al)@PLA indicators was calculated according to Eq. (6) (Teymouri et al., 2025)

$$MA = \frac{Wt - Wi}{Wi} \times 100 \quad (6)$$

Additionally, the color stability (ΔE) of the $NH_2$-MIL-53(Al)@PLA indicators was also evaluated according to Eq. (3) after moisture absorption.

#### 2.4.7. Antibacterial properties

The antibacterial efficacy of the $NH_2$-MIL-53(Al)@PLA indicator against *E. coli* (*ATCC 8739*) and *Staphylococcus aureus* (*ATCC 6538*) was evaluated using a modified agar well diffusion assay (Ahmed et al., 2024; Razavi-Tehrani & Shekarchizadeh, 2026). Initially, the bacterial strains were cultured in Luria–Bertani (LB) broth at 37 °C for 24 h. The concentration of the bacterial suspensions was adjusted to a final density of $10^5$ CFU/mL based on standard plate counts correlated with optical density ($OD_{600}$) measurements. Subsequently, a 100 μL aliquot of each standardized inoculum was uniformly spread onto nutrient agar plates using a sterile cell spreader. Cylindrical wells (5 mm in diameter) were

then aseptically punched into the center of each agar plate. Prior to introduction, all tested specimens were sterilized via UV irradiation for 30 min. Standardized, identical portions of neat PLA and $NH_2$-MIL-53 (Al)@PLA composite films (5 mm in diameter, 0.05 g) were prepared and carefully loaded into the wells. Neat PLA film fragments served as negative controls, whereas equal masses of ciprofloxacin (0.05 g) introduced into separate wells were employed as positive controls. Following aerobic incubation at 37 °C for 24 h, the antimicrobial activity was quantitatively determined by measuring the total diameter of the clear inhibition zones formed around the wells using a digital caliper. All assays were conducted in independent replicates to ensure statistical validity.

#### 2.4.8. Color stability and post-storage sensing efficiency

The color stability of the indicators was evaluated over 10 days at various time intervals (0, 2, 4, 6, 8 and10 days) under different storage temperatures (−18, 4, and 25 °C) in a desiccator (76% RH), following the method of Mohammadalinejhad et al. (2020). To assess the effect of storage on sensing performance, the films stored for 10 days were placed inside sealed glass vials containing 10 mL of a 20 μM aqueous ammonia solution. After 60 s of headspace exposure, the color parameters (L*, a*, and b*) were remeasured, and the total color difference (ΔE) was calculated according to Eq. (3).

#### 2.4.9. Migration

To evaluate the migration behavior of the $NH_2$–MIL-53(Al)@PLA indicators, migration tests were performed according to EU Regulation No 10/2011 and the method reported by Kathuria et al. (2018) with slight modifications. Indicator specimens (2.5 × 2.5 $cm^2$) were completely immersed in 50 mL of different food simulants, including distilled water, 3% (v/v) acetic acid, 10% (v/v) ethanol, and sunflower oil, and subsequently incubated at 40 °C. The leaching of $Al^{3+}$ ions from the indicators into the respective simulants was quantified using inductively coupled plasma optical emission spectroscopy (ICP–OES; Vista-PRO Simultaneous ICP-OES, Varian Inc., Australia). Based on preliminary trials and previous literature, a maximum migration period of 200 h was selected, as ICP–OES screening indicated that $Al^{3+}$ release had fully reached equilibrium under the evaluated conditions.

### 2.5. Evaluation of fish freshness using $NH_2$-MIL-53(Al)@PLA colorimetric indicator

Fresh trout was obtained from the local market and processed immediately. After slaughter, 50 g fish fillet pieces were placed in sterile Petri dishes, each containing one $NH_2$-MIL-53(Al)@PLA colorimetric indicator. To minimize gas exchange with the environment, the dishes were completely sealed with cellophane. The color changes of the indicator were measured using a colorimeter. The fish samples were divided into two storage conditions: one group was kept at room temperature (25 °C) and examined every 6 to 10 h for 60 h, while the other group was stored in a refrigerator (4 °C) and evaluated daily for 11 days (Teymouri et al., 2025).

### 2.6. Fish spoilage characterization

#### 2.6.1. pH measurement

To assess fish spoilage, 5 g of fresh fish meat was homogenized with 45 mL of distilled water for one minute. The pH of the resulting mixture was then measured at room temperature using a calibrated pH meter (Jenway 3330, England) (Gram et al., 2002).

#### 2.6.2. Total volatile basic nitrogen (TVB-N)

Five grams of homogenized fish tissue were transferred into a Kjeldahl flask, followed by the addition of 2 g of magnesium oxide. The TVB-N content was expressed as mg N/100 g of sample (Cheng et al., 2017).

#### 2.6.3. Total viable count (TVC)

The TVC of the fish samples was assessed using the pour plate technique. For this purpose, 10 g of fish tissue was transferred into a sterile flask containing 90 mL of 0.85 % sodium chloride solution and homogenized using a mechanical blender. The homogenate was subsequently subjected to a series of tenfold serial dilutions (v/v) with the same saline solution. From each dilution, 1 mL was aseptically transferred onto the surface of plate count agar in Petri dishes and incubated at 35 °C for 3 days. The microbial load was expressed as colony-forming units (CFU) per gram of the fish sample (Ghaly et al., 2010).

### 2.7. Statistical analysis

Analysis of variance (ANOVA), followed by Fisher's least significant difference (LSD) test at a significance level of $p < 0.05$, was performed using SAS software version 9. All experiments were performed in triplicate, and the results were reported as the mean ± standard deviation. The graphs and charts were plotted using Origin 2025 software to visualize the trends and differences among the treatments.

## 3. Results and discussion

### 3.1. Characterization of $NH_2$-MIL-53(Al)

#### 3.1.1. SEM analysis

The surface morphology of the synthesized materials was characterized via FE-SEM, and statistical particle size distributions were quantified using ImageJ software based on 108 individual particles selected from multiple distinct micrographs to ensure reproducibility (Fig. 1). The pristine $NH_2$-MIL-53(Al) exhibits a homogeneous, granular morphology composed of densely packed and interconnected nanoscale crystallites (Fig. 1a), yielding an average particle size of 142.87 ± 95.84 nm (Fig. 1b). Upon exposure to volatile fish spoilage gases (Fig. 1c), a clear morphological transformation is observed; the initial nanoscale grains evolve into short, well-faceted blocky monoclinic prisms, and the average particle size increases significantly to 5.90 ± 5.60 μm (Fig. 1d).

This wide particle size distribution and the pronounced particle clustering are primarily adsorption-induced phenomena occurring during and after exposure to volatile spoilage amines. Prior to gas exposure, the highly dispersed $NH_2$-MIL-53(Al) nanoparticles offer an abundant and unobstructed external surface area, ensuring rapid gas diffusion and immediate interaction with the active sensing sites ($Al^{3+}$ coordination centers and amino functional groups). As the adsorption process progresses, the co-adsorption of a complex, heterogeneous mixture of spoilage volatiles (including ammonia, trimethylamine, dimethylamine, and sulfur-containing species) triggers intense host–guest interactions and extensive intermolecular hydrogen bonding. Variations in molecular size, polarity, and interaction strengths of these multi-component gases lead to non-uniform localized adsorption within the MOF channels, prompting compact crystallite clustering and surface structural rearrangements.

In contrast, when exposed to pure ammonia gas (Fig. 1e), $NH_2$-MIL-53(Al) displays a highly ordered, anisotropic morphological evolution, transforming into well-oriented, elongated monoclinic rod-like structures with an average size of 0.62 ± 0.61 μm (Fig. 1f). The small kinetic diameter, high polarity, and strong basicity of $NH_3$ facilitate rapid intra-channel diffusion, triggering intense hydrogen bonding with -$NH_2$/carboxylate groups and Lewis acid–base coordination with unsaturated $Al^{3+}$ sites. These localized host–guest interactions induce controlled framework distortions, prompting preferential crystal growth along specific crystallographic directions (Boulé et al., 2018).

The structural divergence between the two exposure states indicates that while pure $NH_3$ predominantly induces oriented crystal restructuring via the framework's flexible breathing behavior—mediating a reversible narrow-pore (np) to large-pore (lp) transition—the complex fish spoilage headspace heavily favors macromolecular interparticle

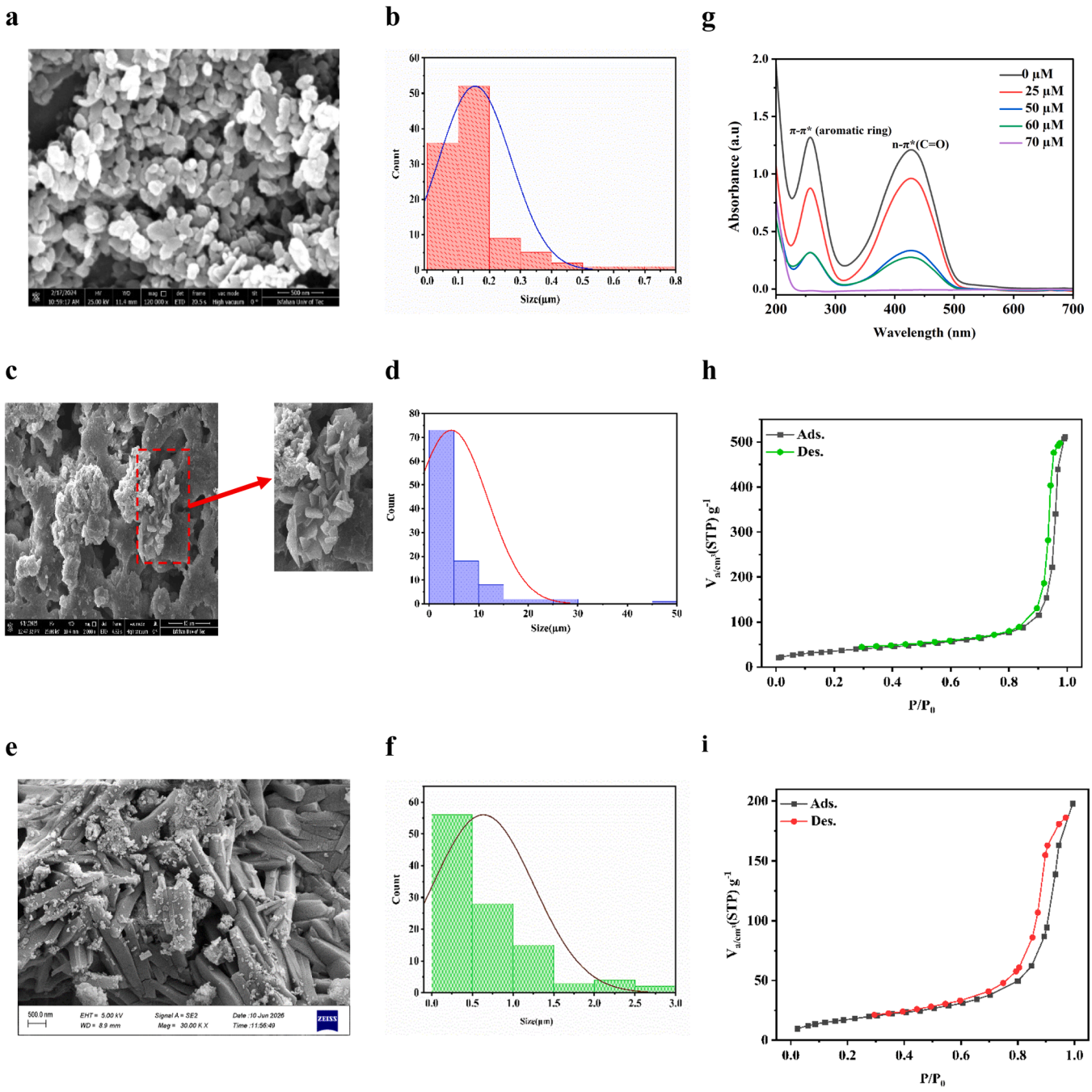


**Fig. 1.** FE-SEM image (a) and particle size distribution (b) of pristine $NH_2$–MIL-53(Al). FE-SEM image (c) and particle size distribution (d) of $NH_2$–MIL-53(Al) after 60 h exposure to gases generated during fish spoilage. FE-SEM image (e) and particle size distribution (f) of $NH_2$–MIL-53(Al) after exposure to $NH_3$ gas. UV–vis absorption spectra (g) of $NH_2$–MIL-53(Al) at different ammonia concentrations. $N_2$ adsorption–desorption isotherm of pristine $NH_2$–MIL-53(Al) with permission from Elsevier (Habibabadi et al., 2026) (h), and $NH_2$–MIL-53(Al) after exposure to fish spoilage gases (i).

aggregation. Because the bulk coordination framework remains unaltered, this apparent enlargement is ascribed to a surface-driven physical aggregation and framework breathing process rather than lattice degradation or phase transformation. These FE-SEM observations are strongly supported by the subsequent XRD and BET analyses; the sharp decline in surface area and pore volume directly validates host–guest pore obstruction, while the unaltered long-range XRD reflections confirm the preservation of the crystalline lattice. Importantly, although this post-exposure aggregation restricts the final accessible internal surface parameters, it does not compromise the overall sensing performance, as the colorimetric transition is successfully initiated at the highly active initial stage of gas-solid contact. Collectively, these multi-scale morphological variations highlight the exceptional chemical sensitivity and structural responsiveness of $NH_2$-MIL-53(Al) toward volatile basic markers, confirming its efficacy for intelligent food packaging.

### 3.1.2. *Visual colorimetric response and UV–vis spectroscopy*

The ammonia-responsive colorimetric behavior of $NH_2$-MIL-53(Al) was investigated by exposing the framework to volatile $NH_3$. As illustrated in Fig. S2, the pristine material displayed a light-yellow appearance, which visibly transitioned into a distinct brownish-yellow shade upon ammonia exposure. This visual response is attributed to intense host–guest interactions between $NH_3$ molecules and the $NH_2$-MIL-53(Al)

framework, encompassing hydrogen bonding with the amino groups and Lewis acid–base coordination with the unsaturated $Al^{3+}$ sites. These interactions modulate the electronic structure surrounding the metal nodes and organic linkers, thereby altering the light absorption profile and inducing a macroscopic color shift (Xu et al., 2023). This pronounced naked-eye responsiveness confirms the suitability of $NH_2$-MIL-53(Al) for monitoring volatile basic nitrogen compounds generated during fish spoilage. To further elucidate the fundamental origin of this colorimetric response and investigate the associated electronic transitions, UV–vis diffuse reflectance spectroscopy was subsequently performed.

The UV–vis spectra of $NH_2$-MIL-53(Al) upon exposure to different concentrations of ammonia gas are shown in Fig. 1g In its initial state, the $NH_2$-MIL-53(Al) sample exhibits two prominent absorption bands. A strong band near 250 nm corresponds to $\pi\rightarrow\pi^*$ electronic transitions associated with aromatic rings, while a broader band around 430 nm is attributed to $n\rightarrow\pi^*$ transitions, which involve non-bonding electrons in carbonyl groups and are modified by the amino-functionalized framework, which modulate the local electronic environment and frontier orbital energies (Li et al., 2025).

The UV–vis spectra of $NH_2$-MIL-53(Al) exposed to varying concentrations of ammonia gas exhibit a progressive decrease in the intensity of the characteristic absorption bands, approaching the baseline at higher concentrations. With increasing ammonia concentration, both the $\pi\rightarrow\pi^*$ and $n\rightarrow\pi^*$ absorption bands gradually weaken, nearly disappearing at 70 μM, indicating a pronounced quenching effect. This attenuation is primarily driven by the interaction of ammonia molecules with the amino-functionalized framework, which alters the local electronic environment of the MOF. Specifically, ammonia can donate lone-pair electrons to the amino groups or coordinate with the framework metal centers, leading to perturbation of the electron density in the conjugated π systems and carbonyl-containing domains. These interactions effectively reduce the oscillator strength of the $\pi\rightarrow\pi^*$ and $n\rightarrow\pi^*$ transitions by modifying the energy gap between the frontier molecular orbitals (HOMO–LUMO), resulting in fewer optically active sites (Al-Qahtani et al., 2026). Consequently, the marked decrease in absorbance reflects the strong electronic coupling between ammonia and the $NH_2$-MIL-53(Al) framework, confirming its high sensitivity and suitability as an efficient optical sensor for ammonia detection.

### 3.1.3. Adsorption and desorption analysis

The surface area, average pore diameter, and pore volume results for the synthesized $NH_2$-MIL-53(Al) before and after exposure to fish spoilage gases are presented in Table 1 and Fig. 1h and i. According to our previous characterization study (Habibabadi et al., 2026), the pristine material exhibits a Type V nitrogen adsorption–desorption isotherm with an H3-type hysteresis loop according to the IUPAC classification, indicating the presence of mesoporous domains and relatively weak adsorbent–adsorbate interactions. In contrast, following exposure to fish spoilage gases, the isotherm profile transitions to a Type III profile with an H1-type hysteresis loop, indicating a substantial alteration in the pore environment and localized mass transport behavior. This transition corresponds to a significant reduction in both BET surface area (from 126.580 to 61.073 $m^2\ g^{-1}$) and pore volume (from 0.786 to 0.302 $cm^3\ g^{-1}$). Similar reductions in textural parameters have been reported across several MOF systems following host–guest pore occupation. For instance, in PtCo/Cr-BDC, the surface area and pore volume dropped due to partial pore obstruction by embedded nanoparticles (Zahid et al., 2023). Likewise, Pt-loaded Ti-MOF catalysts experienced a notable decrease in accessible surface parameters following successful active-phase incorporation within the porous cavities (Dong et al., 2025; Zahid et al., 2024).

**Table 1**
BET results of the $NH_2$-MIL-53(Al) before and after exposure to fish spoilage gases.

| Sample | Pore Volume ($cm^3/g$) | Average Pore Diameter (nm) | Surface Area ($m^2/g$) |
|---|---|---|---|
| $NH_2$-MIL-53(Al) before reaction | 0.786 | 24.829 | 126.580 |
| $NH_2$-MIL-53(Al) after reaction | 0.302 | 19.771 | 61.073 |

The marked decrease in nitrogen adsorption capacity after exposing $NH_2$-MIL-53(Al) to biogenic spoilage gases is primarily driven by three synergistic factors. First, volatile amines and ammonia strongly—and often irreversibly—bind within the open cavities, leading to extensive pore blocking and physical restriction of nitrogen molecules. Second, the adsorption of these polar guest species induces a structural expansion of the flexible $NH_2$-MIL-53(Al) framework. Although this breathing behavior is well-documented, it localizedly narrows specific windows, ultimately reducing the accessible pore volume available for $N_2$ diffusion (Sorribas et al., 2016). Finally, the concurrent aggregation of primary MOF nanoparticles during gas-solid contact drastically limits the free contact surface area. These cumulative structural transformations decrease the effective number of active open pores and overall surface parameters.

## 3.2. Characterization of $NH_2$-MIL-53(Al)@PLA colorimetric indicator

### 3.2.1. Chemical structure

FTIR–ATR spectra of the $NH_2$-MIL-53(Al)@PLA indicator before and after exposure to fish spoilage gases are shown in Fig. 2A. In the pristine $NH_2$-MIL-53(Al) (Fig. 2A (a)), the intense and sharp band at ~771 $cm^{-1}$ is attributed to Al–O stretching vibrations within the characteristic $AlO_4(OH)_2$ chains of the MIL-53 framework, serving as a fingerprint of the structure. The asymmetric and symmetric stretching vibrations of carboxylate groups ($-COO^-$) appear at ~1590 and 1394–1439 $cm^{-1}$, respectively, confirming successful coordination of the $NH_2$–BDC linker to $Al^{3+}$ centers. The broad absorption centered around 3387 $cm^{-1}$ originates corresponding to the N–H stretching modes. Notably, the sharp $\mu_2$-OH stretching band typically expected around 3700 $cm^{-1}$ in MIL-53 frameworks is completely absent. Instead, only a very weak and diffuse background absorption is detectable around 3000 $cm^{-1}$, which is attributed to the framework $\mu_2$-hydroxyl groups that have undergone significant red-shifting and broadening due to medium-strength hydrogen bonding with the adjacent $-NH_2$ functionalities (Rahimpoor et al., 2022). This dramatic suppression and displacement of the hydroxyl vibration serves as strong evidence of effective amino-functionalization and intramolecular hydrogen-bonding interactions within the $NH_2$–MIL-53(Al) structure (Couck et al., 2009; Loiseau et al., 2004; Serra-Crespo et al., 2012).

After exposure to fish spoilage gases (Fig. 2A(b)), remarkable spectral variations are observed. The Al–O band at 771 $cm^{-1}$, along with additional framework-related vibrations below 1000 $cm^{-1}$, significantly decreases in intensity, indicative of strong coordinative adsorption of volatile amines/ammonia onto open $Al^{3+}$ sites and possible pore blockage. The carboxylate stretching bands at 1394 and 1439 $cm^{-1}$ broaden and shift to lower wavenumbers, suggesting perturbation of the Al–carboxylate coordination environment via hydrogen bonding and Lewis's acid–base interactions with nitrogenous volatiles. Concurrently, the broad N–H/O–H region exhibits notable broadening and red-shifting, providing clear evidence of enhanced hydrogen bonding between adsorbed amines and $-NH_2$ groups of the framework (Zhang et al., 2020). Similar FTIR spectral variations have been documented for Fe-L-citrulline (Fe-CIT) and copper-L-tyrosine (Cu-LTE) based metal–organic frameworks upon exposure to volatile ammonia markers. In the case of Fe-CIT, distinct modifications within the N–H, carboxylate, and metal–ligand coordination bands were directly correlated with localized variations in the chemical bonding environment (Li et al., 2024). Similarly, for Cu-LTE, noticeable shifts in the characteristic N–H/O–H stretching and Cu–O network bands were primarily attributed to

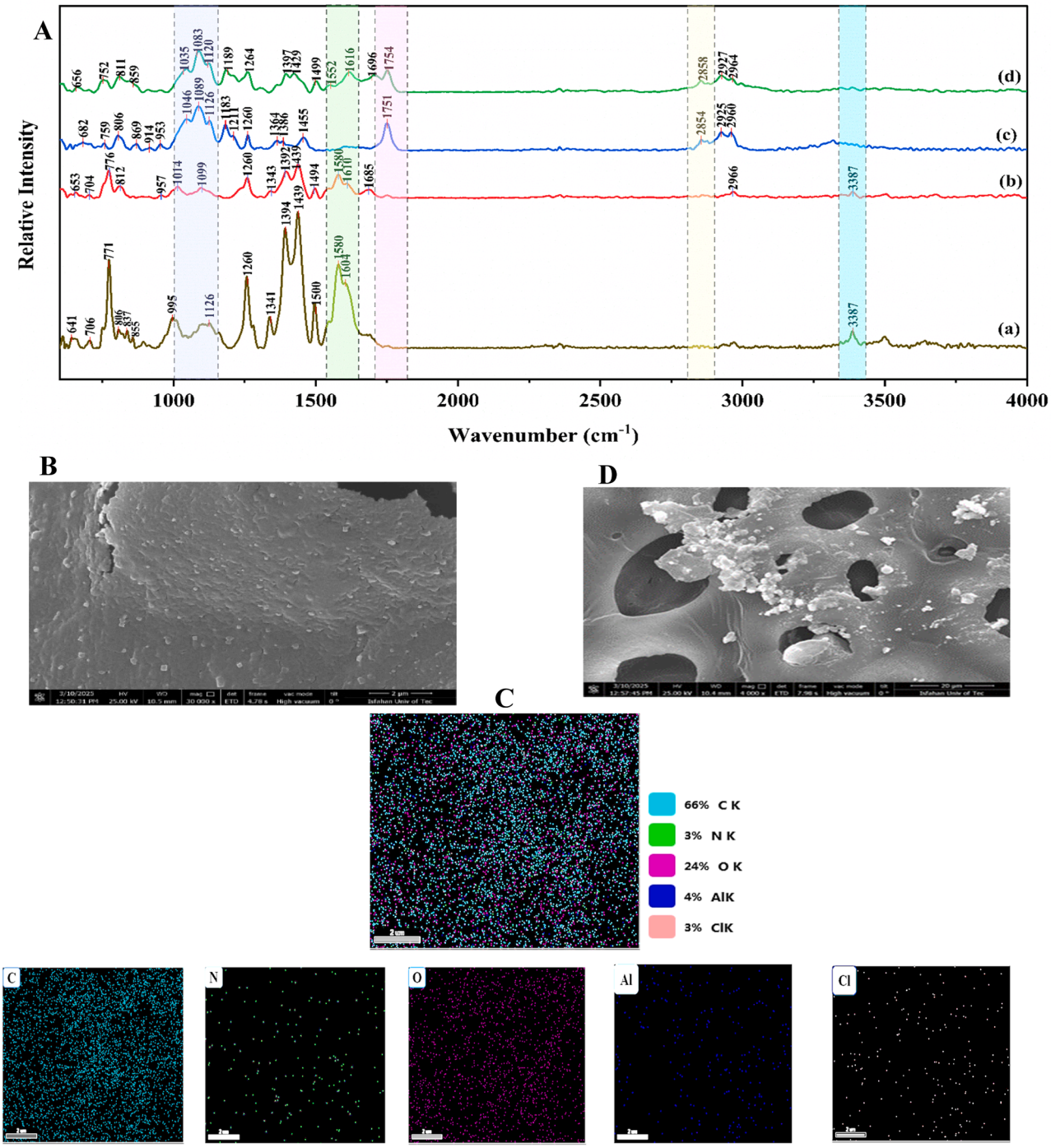


**Fig. 2.** A: FTIR–ATR spectrum of $NH_2$–MIL-53(Al) (a) $NH_2$–MIL-53(Al) after exposure to ammonia gas (b) $NH_2$–MIL-53(Al)@PLA (c) $NH_2$–MIL-53(Al)@PLA after exposure to ammonia gas (d); B. FE-SEM images of the $NH_2$-MIL-53(Al)@PLA before exposure to fish spoilage gases; C; Elemental mapping (EDS) of $NH_2$–MIL-53(Al) @PLA, showing the distribution of the constituent elements C, O, N, Al, and Cl; FE-SEM images of the $NH_2$-MIL-53(Al)@PLA after exposure to fish spoilage gases(D).

extensive hydrogen-bonding interactions with incoming gaseous ammonia molecules (Xia et al., 2025). These literature precedents strongly support our findings, corroborating that the synchronized N–H/O–H transformations observed for $NH_2$–MIL-53(Al) in the current study are predominantly driven by continuous hydrogen-bonding networks and dynamic alterations in the localized electronic environment induced during exposure to complex volatile fish spoilage headspaces.

In the $NH_2$–MIL-53(Al)@PLA composite prior to gas exposure (Fig. 2A(c)), the intensity of MIL-53-specific bands, particularly at 771 $cm^{-1}$ and in the 1400–1600 $cm^{-1}$ region, is substantially reduced due to partial embedding and physical shielding of MOF particles by the polymer matrix. Distinct PLA signatures appear, including C–O–C stretching (1046–1189 $cm^{-1}$), carbonyl stretching at ~1750 $cm^{-1}$, and C–H stretching at 2854 and 2964 $cm^{-1}$. Slight broadening and reduced intensity of the ~3387 $cm^{-1}$ band indicate hydrogen-bonding interactions between $–NH_2$ groups of the MOF and carbonyl moieties of PLA, reflecting good interfacial compatibility and structural preservation of the framework within the composite.

In the $NH_2$–MIL-53@PLA composite after exposure (Fig. 2A(d)), the MOF-related bands exhibit further attenuation, with the characteristic 771 $cm^{-1}$ peak almost completely suppressed, indicating substantial disruption of framework vibrational modes upon interaction with

spoilage gases. Additionally, the N–H/O–H stretching region displays more pronounced broadening and red-shifting compared to the pristine MOF, reflecting intensified hydrogen-bonding interactions with adsorbed nitrogenous species. Minor broadening and slight red-shifting of the PLA carbonyl band further suggest weak but detectable interactions between volatile amines and the polymer matrix. Collectively, these spectral changes confirm stronger and more irreversible adsorption of fish spoilage volatiles by the composite, arising from synergistic mechanisms including coordinative binding at aluminum sites, hydrogen bonding at amino functionalities, and secondary adsorption within the PLA matrix. These findings highlight the chemical sensitivity, structural adaptability, and potential applicability of $NH_2$–MIL-53(Al) and $NH_2$–MIL-53@PLA as effective sensing materials for real-time detection of fish spoilage gases (Wu et al., 2022; Mihaylov et al., 2016).

### 3.2.2. *FE-SEM*

The surface morphology of the $NH_2$–MIL-53(Al)@PLA composite indicator (Fig. 2B) reveals a relatively smooth and continuous structure, with $NH_2$–MIL-53(Al) particles evenly dispersed throughout the PLA matrix. This uniform distribution indicates effective blending of the MOF within the polymer, which is essential for the functional performance of the composite as an intelligent packaging or sensing indicator. The absence of significant agglomeration or large surface defects demonstrates good interfacial compatibility, likely facilitated by hydrogen bonding between amino groups on the MOF surface and the ester groups of PLA, as reported in similar MOF–polymer composites (Cheng et al., 2013). This observation is further supported by the EDS elemental mapping (Fig. 2C), which reveals a homogeneous spatial distribution of aluminum (Al), the characteristic element of the $NH_2$–MIL-53(Al) framework, throughout the PLA matrix. The absence of localized regions with high Al intensity confirms that the MOF particles are uniformly dispersed within the polymer without significant agglomeration. Furthermore, the semi-quantitative EDS analysis showed approximately 4 wt% Al, which is consistent with the intended MOF loading and confirms the successful incorporation and homogeneous integration of $NH_2$–MIL-53(Al) into the polymer matrix.

Following exposure to fish spoilage gases (Fig. 2D), notable changes are observed in the indicator's surface characteristics: increased surface roughness, the formation of distinct pores, and the aggregation of particles. These morphological alterations can be primarily attributed to the

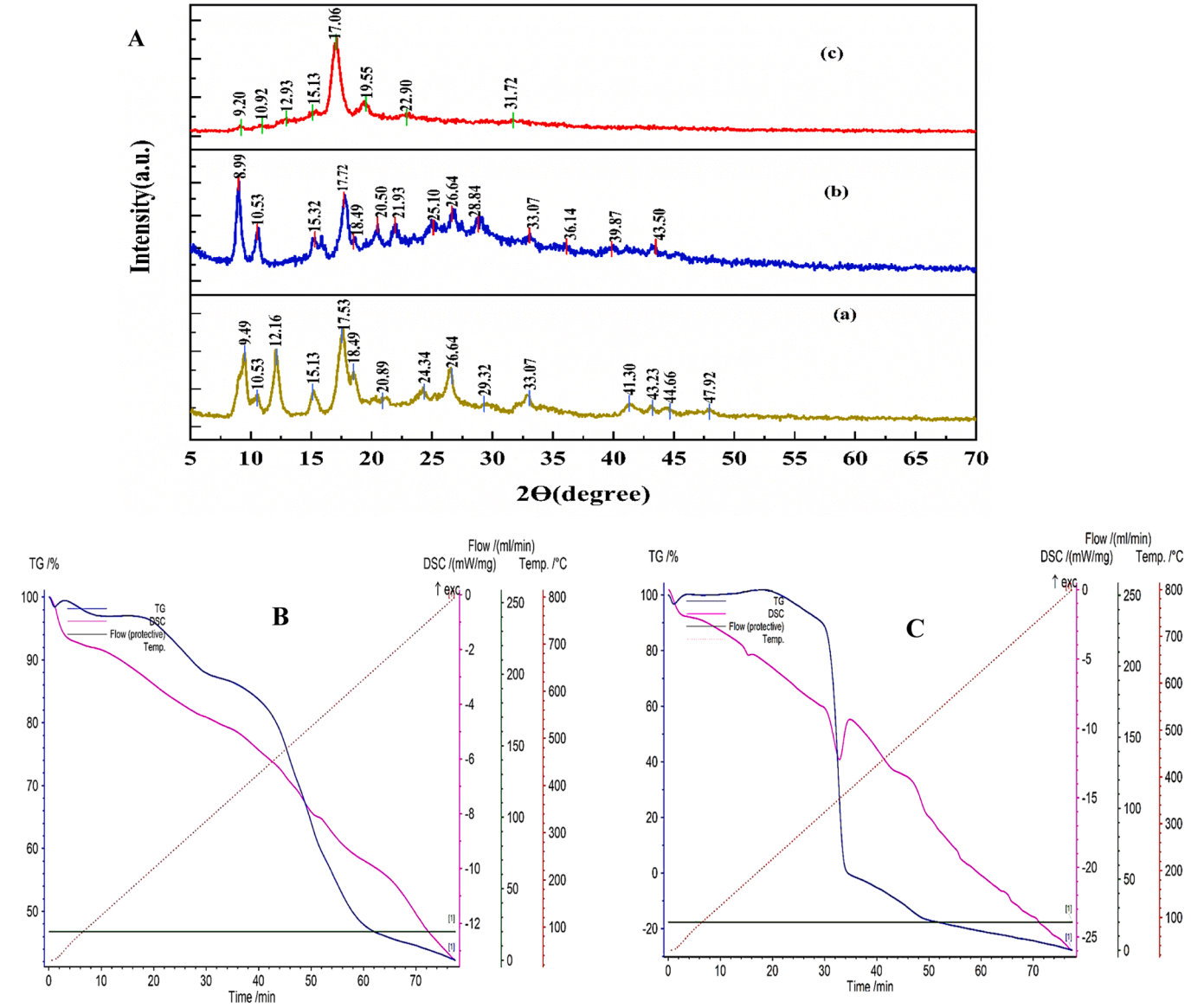


**Fig. 3.** A: XRD pattern of $NH_2$–MIL-53(Al) (a), $NH_2$–MIL-53(Al) after exposure to ammonia gas (b), and $NH_2$–MIL-53(Al)@PLA (c). B: TGA and DSC of $NH_2$–MIL-53 (Al). C: TGA and DSC of $NH_2$–MIL-53(Al)@PLA.

adsorption of volatile amine compounds such as ammonia and other basic gases released during spoilage. The flexible framework of $NH_2$–MIL-53(Al) undergoes structural expansion (the "breathing effect") in response to guest molecule uptake, inducing internal stress and leading to partial disruption of the polymer matrix at the MOF–PLA interface. Such gas-triggered expansion is known to create microvoids and surface undulations in composite matrices (Van Tran et al., 2023)

Additionally, the mildly alkaline environment caused by spoilage gases can promote localized hydrolysis and mild surface degradation of the indicator, as evidenced by perforations and pore development on the indicator's surface. The observed interplay between morphological transformation and gas exposure provides supporting evidence for the indicator's suitability as a gas-responsive indicator material, supporting its application in intelligent food packaging and real-time spoilage detection systems (Wu et al., 2022).

### 3.2.3. Crystalline structure

The XRD pattern of the synthesized $NH_2$-MIL-53(Al) displayed well-defined characteristic reflections at 2θ values of 9.49°, 10.53°, 12.16°, 15.13°, 17.53°, 24.34°, and 26.64° (Fig. 3A(a)). These peaks correspond to the (011), (200), (020), (002), (110), (013), and (040) crystallographic planes, respectively, confirming the successful formation of the amino-functionalized MIL-53 framework (Gecgel et al., 2022; Noorani & Mehrdad, 2023). The absence of unindexed peaks verified the high phase purity of the product, while the broad nature of the reflections reflects the flexible, open-pore breathing characteristics of the framework (Han et al., 2025).

Upon exposure to volatile $NH_3$ gas, the primary diffraction peak shifted slightly from ≈ 9.49° to 8.99°, accompanied by minor intensity fluctuations (Fig. 3A(b)). This behavior is a hallmark of the structural breathing effect in $NH_2$-MIL-53(Al), where guest molecule adsorption induces reversible pore expansion or contraction without framework degradation. This lattice flexibility stems from variations in Al–O bond angles and host–guest interactions induced by polar amine molecules (Van Tran et al., 2023). These findings corroborate the FE-SEM observations, which showed surface morphological alterations while the long-range crystalline order remained intact. Complementarily, FTIR analysis (Fig. 2A(b)) captured local electronic and hydrogen-bonding rearrangements between $NH_3$ and the -$NH_2$ or metal sites, confirming local chemical coordination without disrupting the bulk crystalline lattice (Jiang et al., 2025).

In the $NH_2$–MIL-53(Al)@PLA pattern (Fig. 3A(c)), the diffractogram confirms the coexistence of both the polymer matrix and the MOF. Specifically, the weak characteristic reflections of $NH_2$–MIL-53(Al) at 2θ ≈ 9.20°, 10.92°, and 15.13° are preserved, albeit with reduced intensity due to the dilution effect within the polymer network. Meanwhile, the predominant and sharp reflection appearing at 2θ ≈ 17.06° is associated with the semi-crystalline structure of PLA, indexing to the α-phase (110)/(200) planes (Hsieh et al., 2020). The incorporation of $NH_2$–MIL-53(Al) particles provides heterogeneous nucleation sites for PLA, promoting a more ordered arrangement of polymer chains during film formation (Abid et al., 2018; Dai et al., 2016). Ultimately, the preservation of these combined diffraction features demonstrates the structural integrity of both phases and the successful incorporation of the MOF into the PLA matrix.

### 3.2.4. Thermal stability

The thermal behavior of pristine $NH_2$-MIL-53(Al) and the $NH_2$-MIL-53(Al)@PLA composite film was investigated simultaneously via TGA and DSC (Fig. 3B and C). For pristine $NH_2$-MIL-53(Al) (Fig. 3B), a multi-step weight loss profile was recorded. A minor weight loss below 150 °C corresponds to the desorption of physically adsorbed water and residual solvent trapped within the porous network (Huang et al., 2021). The framework exhibited remarkable thermal stability up to approximately 450 °C. A sharp weight loss event occurred between 450 and 550 °C, driven by the thermal decomposition of the 2-aminoterephthalate organic linkers. Beyond this range, the weight stabilized due to the formation of inorganic aluminum oxide residues. The DSC thermogram strongly supported these findings, displaying three distinct endothermic peaks at 474.0, 544.0, and 696.1 °C. The first two peaks coincide with the progressive collapse of the organic linkers, while the final peak at 696.1 °C is assigned to the phase transition and stabilization of aluminum oxides.

The $NH_2$-MIL-53(Al)@PLA indicator exhibited a distinct multi-stage degradation profile (Fig. 3C). The initial weight loss below 150 °C (∼8%) is attributed to the release of moisture adsorbed within the embedded MOF pores, which correlates with a broad endothermic DSC signal in the same region. A minor thermal event near 179 °C is ascribed to the melting or relaxation processes of the PLA matrix. The primary degradation stage occurred rapidly between 330 and 380 °C, resulting in an 86% mass drop. This is accompanied by a pronounced endothermic DSC peak centered at ∼353 °C, signaling the thermal depolymerization of the PLA backbone (Segura González et al., 2018). In the final stage (400–800 °C), a continuous, gradual weight loss reflects the delayed decomposition of the remaining $NH_2$-MIL-53(Al) framework. The higher decomposition temperature of the MOF relative to the polymer matrix demonstrates that the filler retains its structural integrity beyond the processing and degradation limits of PLA. Ultimately, these results confirm that $NH_2$-MIL-53(Al) is fully compatible with PLA and highly suitable for intelligent food packaging applications.

### 3.2.5. Thickness and mechanical properties

The thickness of the indicators significantly increased following the incorporation of $NH_2$-MIL-53(Al), demonstrating that the MOF fillers influenced the structural organization of the polymer matrix (Table S1, Supplementary Information). This increase can be attributed to the introduction of porous particles, which enhanced the overall solid content and occupied additional volume within the polymer network. Moreover, the presence of $NH_2$-MIL-53(Al) likely interfered with the compact packing of PLA chains during solvent evaporation. Specifically, the amino groups of $NH_2$-MIL-53(Al) can form hydrogen bonds with the carbonyl groups of PLA, thereby restricting chain mobility and preventing matrix densification. Furthermore, the highly porous framework and large specific surface area of the MOF may increase the free volume within the composite structure, contributing to the formation of thicker films. These findings are in excellent agreement with a recent study by Huang et al. (2025), who reported that incorporating MIL-53-$NH_2$ into a poly(vinyl alcohol) matrix increased the film thickness to 0.172 ± 0.009 mm compared to the neat PVA control. This increase was directly attributed to the intercalation of MOF particles within the polymeric network, resulting in structural expansion and increased intermolecular distance between the polymer chains.

The incorporation of $NH_2$–MIL-53(Al) into the PLA matrix significantly affected the mechanical properties of the resulting composite indicator (Table S1, Supplementary Information). Specifically, both tensile strength and elongation at break decreased for the $NH_2$–MIL-53(Al)@PLA indicator, indicating a substantial increase in the brittleness of the composite structure. This behavior can be attributed to the presence of amino functional groups in $NH_2$–MIL-53(Al), which are capable of forming hydrogen-bonding interactions with the ester carbonyl groups of PLA. Although these interactions improve the interfacial compatibility between the MOF particles and the polymer matrix, they simultaneously restrict the mobility of the PLA molecular chains. This reduced chain mobility limits the ability of the polymer segments to rearrange and dissipate stress under tensile deformation, thereby suppressing plastic deformation and inducing premature fracture (Kathuria et al., 2018).

The observed mechanical behavior is consistent with previous reports on similar systems, such as the study by Dai et al. (2016) on PLA/MOF-508a composites. They reported that an increase in structural ordering and crystallinity of the semi-crystalline PLA matrix resulted in enhanced brittleness and a marked reduction in elongation at break.

This phenomenon was attributed to a greater fraction of crystalline domains, which restrict the mobility of amorphous chain segments and reduce the capacity of the polymer to absorb deformation energy. Further support for this mechanism can be found in a related study by Khezerlou et al. (2023) on guar gum/κ-carrageenan films containing lactoferrin-loaded Cr-MOF. The incorporation of Cr-MOF particles reduced the elongation at break through the formation of additional intermolecular interactions between the functional groups of the MOF and the biopolymer matrix. These interactions generated a denser and more rigid network structure, leading to reduced chain flexibility.

### 3.2.6. Response of $NH_2$-MIL-53(Al)@PLA indicator to pH changes

Table 2 summarizes the colorimetric response of the $NH_2$-MIL-53(Al)@PLA indicator across a wide pH range. The results show that variations in pH did not lead to significant changes in the L*, a*, and b* values. Visual observations were consistent with these measurements, as no noticeable color change was detected across the tested pH range. Although minor statistical fluctuations were observed in the numerical values ($p < 0.05$), they did not have any practical impact on the indicator's appearance. This overall chromatic stability confirms that the $NH_2$-MIL-53(Al)@PLA system does not function as a conventional pH-responsive colorimetric sensor, contrasting sharply with traditional synthetic dyes (e.g., bromocresol green) or natural pigments (e.g., anthocyanins). This behavior is attributed to the absence of labile chromophoric groups capable of undergoing reversible protonation/deprotonation-induced electronic transitions. While the amino groups of the $NH_2$-MIL-53(Al) framework can participate in surface acid–base equilibria, these localized interactions do not perturb the core electronic structure of the framework or alter its optical properties; instead, these functionalities function primarily as active adsorption sites rather than standalone color-generating centers.

Although the $NH_2$-MIL-53(Al)@PLA indicator exhibited a strong correlation with pH changes during real-time fish storage ($R^2 = 0.998$ at room temperature; Section 3.3), this relationship represents an indirect, spoilage-driven co-variation rather than a direct pH-sensing mechanism. During seafood decomposition, the progressive microbial degradation of proteins simultaneously elevates the matrix pH and releases volatile total volatile basic nitrogen (TVB-N) molecules (e.g., ammonia and biogenic amines). Crucially, while post-mortem muscle pH shifts are partially mitigated by the natural buffering constituents of fish flesh (including proteins, peptides, and phosphates), the headspace accumulation of volatile amines remains unbuffered.

Therefore, matrix pH acts purely as a concurrent macro-indicator of spoilage progression, whereas the colorimetric transition of the film is exclusively governed by the active capture of volatile amines within the one-dimensional porous channels of $NH_2$-MIL-53(Al) via hydrogen bonding, host–guest adsorption, and Lewis acid–base coordination. This target-specific affinity aligns with previous reports demonstrating the pronounced responsiveness of amino-functionalized MIL-53 matrices toward volatile basic nitrogen markers (Zhang et al., 2025), which directly modulates the framework's local electronic environment to yield a naked-eye optical response. Ultimately, this intrinsic liquid-pH insensitivity minimizes environmental cross-sensitivity, enhancing the reliability and selectivity of the indicator for practical intelligent packaging applications.

**Table 2**
Colorimetric parameters of the $NH_2$-MIL-53(Al)@PLA indicator in response to pH.

| pH | L* | a* | b* | ΔE | Appearance |
|---|---|---|---|---|---|
| 3 | 65.48 ± 0.11$^{a}$ | 0.09 ± 0.05$^{a}$ | 3.77 ± 0.33$^{bc}$ | 0.25 ± 0.01$^{c}$ |  |
| 4 | 65.46 ± 0.24$^{a}$ | 0.08 ± 0.01$^{a}$ | 2.89 ± 0.22$^{c}$ | 0.90 ± 0.23$^{bc}$ |  |
| 5 | 65.55 ± 0.27$^{a}$ | 0.10 ± 0.06$^{a}$ | 3.72 ± 0.41$^{bc}$ | 0.36 ± 0.02$^{c}$ |  |
| 6 | 65.53 ± 0.43$^{a}$ | 0.12 ± 0.16$^{a}$ | 4.64 ± 0.32$^{ab}$ | 0.93 ± 0.32$^{bc}$ |  |
| 7 | 65.54 ± 0.78$^{a}$ | 0.11 ± 0.04$^{a}$ | 5.82 ± 0.91$^{a}$ | 2.13 ± 0.89$^{a}$ |  |
| 8 | 65.38 ± 0.19$^{a}$ | 0.18 ± 0.03$^{a}$ | 3.69 ± 0.61$^{bc}$ | 0.47 ± 0.14$^{bc}$ |  |
| 9 | 65.59 ± 0.44$^{a}$ | 0.13 ± 0.07$^{a}$ | 5.25 ± 0.73$^{a}$ | 1.51 ± 0.75$^{ab}$ |  |
| 10 | 65.45 ± 0.23$^{a}$ | 0.15 ± 0.17$^{a}$ | 3.60 ± 0.74$^{bc}$ | 0.58 ± 0.22$^{bc}$ |  |
| 11 | 65.37 ± 0.12$^{a}$ | 0.14 ± 0.00$^{a}$ | 4.71 ± 0.81$^{ab}$ | 0.97 ± 0.77$^{bc}$ |  |

Different letters in each column show significant differences between samples ($p < 0.05$).

### 3.2.7. Colorimetric response to ammonia

During the process of fish spoilage, protein degradation caused by microbial and enzymatic activity leads to the release of volatile nitrogenous compounds, particularly ammonia, which can serve as a reliable freshness indicator. The colorimetric response to ammonia is summarized in Table 3, which shows the colorimetric behavior of the $NH_2$-MIL-53(Al)@PLA indicator upon exposure to different ammonia

**Table 3**
Colorimetric parameters of $NH_2$-MIL-53(Al)@PLA indicator in response to ammonia.

| Concentration (μM) | L* | a* | b* | ΔE | Appearance |
|---|---|---|---|---|---|
| 0 | 65.35 ± 0.23$^{a}$ | 0.08 ± 0.06$^{e}$ | 3.55 ± 0.45$^{f}$ | 0.36 ± 0.01$^{f}$ |  |
| 20 | 62.84 ± 0.41$^{b}$ | 0.09 ± 0.02$^{e}$ | 6.21 ± 0.66$^{e}$ | 3.65 ± 0.76$^{e}$ |  |
| 40 | 61.76 ± 1.20$^{b}$ | 1.74 ± 0.72$^{d}$ | 9.31 ± 0.75$^{d}$ | 7.13 ± 1.22$^{d}$ |  |
| 60 | 57.72 ± 0.03$^{c}$ | 5.75 ± 0.15$^{c}$ | 11.54 ± 0.56$^{c}$ | 12.47 ± 0.34$^{c}$ |  |
| 80 | 56.89 ± 0.48$^{c}$ | 7.62 ± 0.43$^{b}$ | 14.50 ± 0.38$^{b}$ | 15.91 ± 0.52$^{b}$ |  |
| 100 | 51.78 ± 0.15$^{d}$ | 9.46 ± 0.67$^{a}$ | 17.58 ± 0.44$^{a}$ | 21.86 ± 0.37$^{a}$ |  |

Different letters in each column show significant differences between samples ($p < 0.05$).

concentrations (0–100 μM). In this study, the $NH_2$-MIL-53(Al)@PLA indicator exhibited distinct and concentration-dependent color changes with increasing ammonia levels. As the ammonia concentration increased, the $NH_2$-MIL-53@PLA indicator displayed a gradual yet visibly noticeable color transition, confirmed by significant ($p \leq 0.05$) variations in the L*, a*, b*, and ΔE values. The lightness (L*) continuously decreased from 65.35 ± 0.23 to 51.78 ± 0.15, indicating a darker color, while the redness (a*) and yellowness (b*) values increased significantly. Consequently, the color of the indicator shifted from an off-white cream tone to brown. Similarly, the total color difference (ΔE) increased from 0.36 ± 0.01 at a concentration of 0 μM to 21.86 ± 0.37 at 100 μM, which clearly exceeded the visual detection threshold, confirming the suitability of the indicator for ammonia detection through visible color observation.

Using the calibration curve with the linear equation $y = 0.208x - 0.437$ (Fig. 4a), the LOD and LOQ were calculated to be 5.24 μM and 15.90 μM, respectively. The equivalent gas-phase LOD and LOQ for ammonia were calculated as 128.12 and 388.76 ppm, respectively. Crucially, these values represent a theoretical, worst-case scenario assuming comprehensive volatilization of the dissolved analyte into the headspace. In a realistic closed-vial configuration, a strict Henry's law partitioning does not fully apply due to the complex, pH-dependent $NH_3/NH^{4+}$ ionic equilibrium, wherein only the non-ionized molecular $NH_3$ fraction can escape into the gas phase. Consequently, a significant portion of the precursor analyte remains trapped in the aqueous medium, meaning that the actual, time-resolved gaseous concentrations required to trigger a macroscopic color change in the indicator are inherently lower than these theoretically calculated thresholds. By reporting these conservative upper-bound limits, a high safety margin is established that confidently encompasses the empirical detection capabilities of the composite films under practical smart packaging environments.

The porous structure of $NH_2$-MIL-53(Al), confirmed by BET analysis, features one-dimensional channels that facilitate rapid $NH_3$ adsorption (Sompornpailin et al., 2022). Ammonia molecules directly interact with the open metal sites within the $NH_2$-MIL-53(Al) network, typically trivalent aluminum ions, forming coordination complexes that alter the electronic environment of the metal–organic framework (MOF). In addition, the presence of electron-rich aromatic linkers in $NH_2$-MIL-53(Al) enables hydrogen bonding and π-electron interactions with ammonia, which further influence the charge distribution within the framework. This cumulative effect leads to changes in the energy band

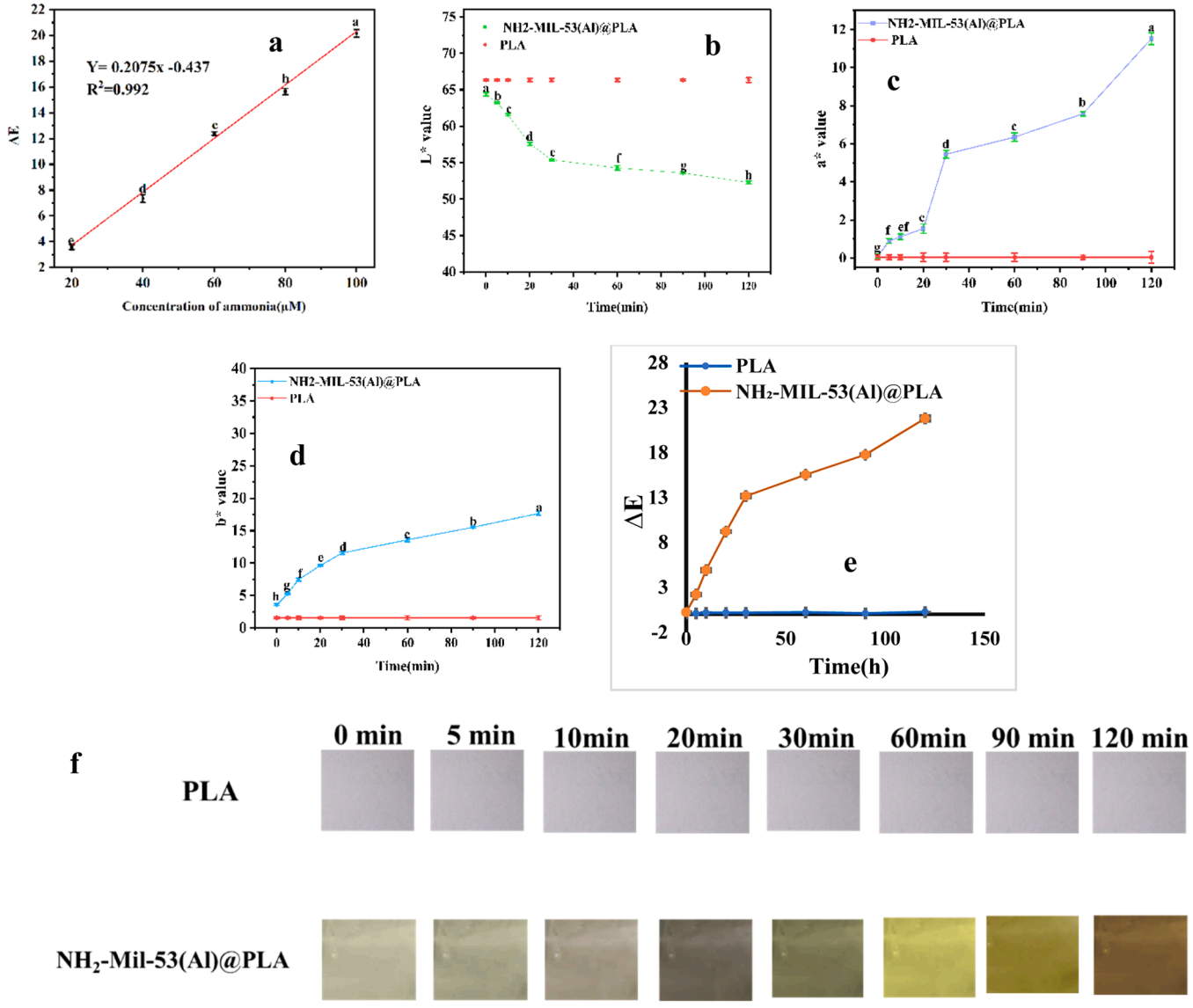


**Fig. 4.** Total color difference (ΔE) of $NH_2$-MIL-53(Al)@PLA at different ammonia concentrations (a); L* (b), a* (c), b* (d), ΔE (e), and appearance (f) of $NH_2$-MIL-53(Al)@PLA at different time of exposure to ammonia.

gap and the light absorption profile of the MOF, ultimately resulting in an observable color change in the indicator. Therefore, the detection mechanism is controlled by a combination of physical adsorption, metal–ligand coordination, and electronic perturbations, all of which contribute to the distinct color variation observed in the $NH_2$-MIL-53 (Al)@PLA indicator.

The results obtained in this project show strong agreement with the findings of Huang et al. (2024), who employed pectin films containing MIL-100(Fe) loaded with anthocyanins (ANs@MIL/P). They reported high sensitivity and faster color changes in the presence of volatile ammonia, which is a key indicator of protein degradation during meat spoilage. The observed color change from purple to bluish-purple and eventually to green was attributed to the interaction of ammonia with water molecules and the formation of ammonium hydroxide ($NH_4OH$), which in turn altered the light absorption characteristics of anthocyanidin compounds (Huang et al., 2024). Furthermore, Watkins et al. showed that amino-functionalized MIL-53(Al) exhibits intra-framework interactions between the $–NH_2$ groups of the linker and the bridging $\mu_2$-OH groups of the inorganic secondary building units. These interactions alter the local coordination environment and thus modulate the framework flexibility and guest adsorption behavior (Serra-Crespo et al., 2012).

The ammonia-sensitive colorimetric indicator based on $NH_2$-MIL-53 (Al) exhibited a distinct and time-dependent color transition from pale white to yellowish-brown after exposure to ammonia vapors for 120 min (Fig. 4b–f). The L* value gradually decreased with increasing exposure time, from 64.36 ± 0.24 to 52.28 ± 0.21 (Fig. 4b). The a* parameter, showed a steady increase from 0.09 ± 0.07 to 11.52 ± 0.32 (Fig. 4c). Similarly, the b* value, increased markedly from 3.55 ± 0.14 to 17.65 ± 0.22 (Fig. 3d) after the initial phase, which was consistent with the visual observations (Fig. 4f). The total color difference (ΔE) (Fig. 4e) increased progressively with increasing ammonia exposure time, confirming the time-dependent response behavior of the $NH_2$-MIL-53(Al)-based indicator. At the initial stage of exposure, ΔE reached 0.22 ± 0.03, indicating the onset of a measurable colorimetric response. After 120 min of exposure, ΔE reached 21.79 ± 0.25, corresponding to a pronounced color change that was readily distinguishable by the naked eye. These results clearly confirm that the $NH_2$-MIL-53(Al)-based colorimetric indicator possesses excellent responsiveness, stability, and visual detectability toward ammonia vapors.

### 3.2.8. Selectivity

As shown in Table 4, the $NH_2$-MIL-53(Al)@PLA indicator demonstrated high selectivity toward volatile nitrogen-containing compounds. Exposure to non-nitrogenous volatiles such as acetic acid, ethanol, and acetone did not produce significant changes in the colorimetric parameters (L*, a*, b*, and ΔE) ($p > 0.05$), indicating minimal interaction between these compounds and the active sites of $NH_2$-MIL-53 (Al)@PLA. In contrast, trimethylamine (TMA), a representative amine generated during protein decomposition, induced a pronounced and statistically significant color change ($p < 0.05$). This behavior confirms both the sensitivity and selectivity of the indicator toward nitrogenous volatiles (Hashemian et al., 2023). The observed selectivity can be attributed to the structural features of $NH_2$-MIL-53(Al), including its highly porous framework, large surface area, and the presence of open metal coordination sites, which facilitate adsorption and hydrogen bonding or Lewis acid–base interactions with electron-rich amine groups. These findings align with previous reports, such as Hashemian et al. (2023), who developed cellulose acetate/MOF films for on-site ammonia detection and highlighted the importance of selectivity, stability, and visual detectability.

**Table 4**
Effect of other volatile compounds on color parameters of $NH_2$-MIL-53(Al) @PLA.

| Concentration (μM) | L* | a* | b* | ΔE | Appearance |
|---|---|---|---|---|---|
| **Acetic acid** | 65.34 ± 0.18$^a$ | 0.05 ± 0.04$^b$ | 5.22 ± 0.12$^b$ | 0.15 ± 0.01$^c$ |  |
| **Ethanol** | 65.35 ± 0.19$^a$ | 0.06 ± 0.03$^b$ | 5.23 ± 0.14$^b$ | 0.17 ± 0.04$^c$ |  |
| **Acetone** | 65.36 ± 0.17$^a$ | 0.08 ± 0.07$^b$ | 4.67 ± 0.55$^b$ | 0.56 ± 0.53$^b$ |  |
| **Trimethylamine** | 52.71 ± 0.50$^b$ | 11.39 ± 0.15$^a$ | 16.49 ± 0.21$^a$ | 20.38 ± 0.09$^a$ |  |

Different letters in each column show significant differences between samples ($p < 0.05$).

### 3.2.9. Moisture absorption

Low moisture absorption is a key prerequisite for colorimetric food packaging indicators, as excess water uptake can induce matrix swelling and adversely alter sensing accuracy. As shown in Fig. 5a, the $NH_2$-MIL-53(Al)@PLA indicator exhibited reduction in moisture absorption compared to neat PLA. Although $NH_2$-MIL-53(Al) possesses an intrinsically porous structure and hydrophilic functional groups, the water uptake of the composite is dictated by the altered transport dynamics within the polymer network (Loiseau et al., 2004). The incorporation of $NH_2$-MIL-53(Al) into the PLA matrix induces strong interfacial interactions between the amino groups of the MOF and the carbonyl groups of PLA, thereby restricting polymer chain mobility and compressing the free volume available for water vapor diffusion. Concurrently, the uniform dispersion of the MOF nanoparticles creates a tortuous pathway for water molecules, effectively obstructing their transverse migration through the film. Similar barrier enhancements were reported by Dorosti and Alizadehdakhel (2018) for MIL-53 (Al)-based Pebax composite membranes. Furthermore, a portion of the penetrating water molecules can be immobilized within the microporous cavities of $NH_2$-MIL-53(Al) as bound water through hydrogen-bonding with -$NH_2$ and Al–OH active sites, preventing them from participating in free water migration or promoting matrix swelling (Singh et al., 2011; Kathuria et al., 2018). Crucially, this localized immobilization indicates that the intrinsic porosity of the MOF remains uncompromised and fully accessible to small, volatile target molecules like ammonia.

To evaluate the impact of humidity on the visual performance of the indicator, the total color difference (ΔE) was tracked over a 9-day period (Fig. 5b). The ΔE values remained nearly constant with no statistically significant variations ($p > 0.05$). This excellent optical stability confirms that the restricted water diffusion and stable interfacial matrix anchoring successfully protect the core color-responsive domains from moisture-induced structural deformation or premature color leaching, demonstrating the indicator's high reliability for humid food packaging environments.

### 3.2.10. Antibacterial properties

In food packaging, functional materials are required to possess antimicrobial activity to suppress microbial proliferation and prolong the shelf life of perishable products. Accordingly, the antibacterial efficiency of the neat PLA and the $NH_2$-MIL-53(Al)@PLA indicators was evaluated against *E. coli* and *Staphylococcus aureus* (Fig. 5c). The neat PLA film exhibited no noticeable antibacterial activity, with negligible inhibition zones of 0.23 ± 0.02 mm for *E. coli* and 0.43 ± 0.04 mm for *S. aureus*, confirming the absence of intrinsic bactericidal properties in the polymer matrix. In contrast, the $NH_2$-MIL-53(Al)@PLA indicator demonstrated significant antibacterial performance, yielding mean

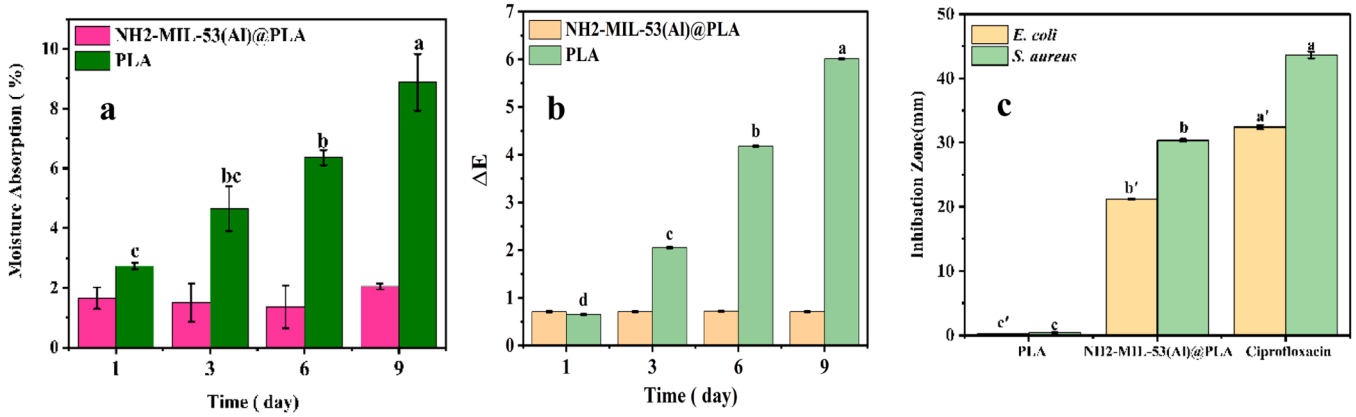


**Fig. 5.** Moisture absorption of $NH_2$-MIL-53(Al)@PLA (a) and its ΔE (b) during time; Antibacterial effect of $NH_2$-MIL-53(Al)@PLA indicator(c).

inhibition zones of 21.20 ± 0.10 mm for *E. coli* and 30.34 ± 0.22 mm for *S. aureus*.

For benchmarking purposes, Ciprofloxacin produced higher inhibition zones of 32.43 ± 0.35 mm against *E. coli* and 43.67 ± 0.51 mm against *S. aureus*. This difference stems from the fact that Ciprofloxacin is a low-molecular-weight, highly diffusible antibiotic that directly targets intracellular DNA replication enzymes (DNA gyrase and topoisomerase IV) (Mason et al., 1995). Conversely, $NH_2$-MIL-53(Al)@PLA is a solid-state material whose activity is primarily governed by a contact-dependent, surface-mediated mechanism rather than bulk leaching. This is supported by the negligible migration of $Al^{3+}$ ions under neutral aqueous conditions (as confirmed by ICP–OES). Instead, the Lewis acidic $Al^{3+}$centers and amino-functionalized linkers on the exposed MOF surfaces undergo electrostatic and coordination-driven interactions with the negatively charged components of the bacterial cell envelope. This intense interfacial contact induces localized membrane rearrangement, structural destabilization, and a subsequent loss of cellular integrity (Fig. S3). A similar surface-controlled pathway was documented by Quiros et al. (2015) for cobalt-based MOF (Co-SIM-1)-loaded PLA electrospun mats, where Live/Dead staining verified that bacterial inactivation occurred predominantly at the material interface rather than in the surrounding medium.

The more pronounced antibacterial efficacy observed against *S. aureus* compared to *E. coli* is attributed to structural variations in their cell envelopes (Arshadi Edlo & Akhbari, 2024). *E. coli* possesses a lipopolysaccharide-rich outer membrane that acts as an effective permeability barrier against hydrophobic or bulky agents. Furthermore, Gram-negative bacteria are equipped with active efflux systems, such as the tripartite AcrAB–TolC transporter, which actively extrudes toxic substances out of the cell, thereby reducing their intracellular accumulation and mitigating overall antibacterial efficacy (Zgurskaya et al., 2015).

### 3.2.11. *Color stability and post-storage responsive behavior*

The color stability of the $NH_2$-MIL-53(Al)@PLA indicators was monitored over 10 days at different temperatures, and the results are summarized in Table 5. The indicators exhibited excellent color stability under refrigerated (4 °C) and frozen (−18 °C) conditions, showing negligible color variations. However, a slightly higher yet acceptable color shift was captured at ambient temperature (25 °C), suggesting that the color transition in real application is primarily triggered by volatile spoilage metabolites rather than intrinsic film instability. This performance aligns with Huang et al. (2025), who reported that incorporating various MOFs into polyvinyl alcohol/corn starch films maintained robust color stability over 15 days under controlled environments.

Importantly, the indicators successfully maintained their ammonia-sensing capability after the 10-day storage period (Table 6). This prolonged functionality is attributed to the stable polymer–MOF interfacial

**Table 5**
Color stability of colorimetric $NH_2$-MIL-53(Al)@PLA indicators.

| Time (day) | | Color parameters | | | |
|---|---|---|---|---|---|
| | | L* | a* | b* | ΔE |
| Freezer | 0 | 65.28 ± 0.37$^{a}$ | 0.17 ± 0.31$^{a}$ | 2.79 ± 0.82$^{b}$ | 0.67 ± 0.00$^{a}$ |
| | 2 | 65.76 ± 0.69$^{a}$ | 0.26 ± 0.10$^{a}$ | 3.74 ± 0.46$^{ab}$ | 1.11 ± 0.70$^{a}$ |
| | 4 | 65.48 ± 0.24$^{a}$ | 0.05 ± 0.20$^{a}$ | 3.72 ± 0.52$^{ab}$ | 0.98 ± 0.51$^{a}$ |
| | 6 | 65.38 ± 0.32$^{a}$ | 0.08 ± 0.19$^{a}$ | 4.71 ± 0.64$^{a}$ | 1.94 ± 0.63$^{a}$ |
| | 8 | 65.93 ± 0.83$^{a}$ | 0.09 ± 0.00$^{a}$ | 3.67 ± 0.92$^{ab}$ | 1.12 ± 0.22$^{a}$ |
| | 10 | 65.95 ± 0.81$^{a}$ | 0.06 ± 0.16$^{a}$ | 4.97 ± 0.42$^{a}$ | 2.33 ± 0.62$^{a}$ |
| Refrigerator | 0 | 65.87 ± 0.60$^{a}$ | 0.14 ± 0.13$^{b}$ | 3.80 ± 0.70$^{a}$ | 0.65 ± 0.02$^{c}$ |
| | 2 | 65.17 ± 0.41$^{a}$ | 0.18 ± 0.04$^{ab}$ | 3.78 ± 0.56$^{a}$ | 0.82 ± 0.36$^{c}$ |
| | 4 | 64.94 ± 0.52$^{a}$ | 0.03 ± 0.01$^{b}$ | 4.76 ± 0.88$^{a}$ | 1.53 ± 0.23$^{ab}$ |
| | 6 | 64.96 ± 0.45$^{a}$ | 0.35 ± 0.02$^{a}$ | 3.73 ± 0.63$^{a}$ | 1.04 ± 0.43$^{bc}$ |
| | 8 | 64.57 ± 0.70$^{a}$ | 0.11 ± 0.12$^{b}$ | 4.91 ± 0.53$^{a}$ | 1.81 ± 0.78$^{a}$ |
| | 10 | 64.55 ± 0.72$^{a}$ | 0.15 ± 0.07$^{b}$ | 4.86 ± 0.54$^{a}$ | 1.80 ± 0.20$^{a}$ |
| Ambient | 0 | 66.33 ± 0.39$^{a}$ | 0.21 ± 0.49$^{a}$ | 5.81 ± 0.58$^{a}$ | 0.64 ± 0.03$^{a}$ |
| | 2 | 66.18 ± 0.47$^{a}$ | 0.29 ± 0.30$^{a}$ | 5.77 ± 0.61$^{a}$ | 0.60 ± 0.07$^{a}$ |
| | 4 | 65.98 ± 0.26$^{ab}$ | 0.22 ± 0.34$^{a}$ | 4.89 ± 0.50$^{a}$ | 1.05 ± 0.49$^{a}$ |
| | 6 | 65.74 ± 0.43$^{ab}$ | 0.23 ± 0.40$^{a}$ | 4.75 ± 0.87$^{a}$ | 1.26 ± 0.92$^{a}$ |
| | 8 | 65.80± 0.44$^{ab}$ | 0.25 ± 0.36$^{a}$ | 5.90 ± 0.62$^{a}$ | 0.79 ± 0.21$^{a}$ |
| | 10 | 64.85 ± 0.73$^{b}$ | 0.27 ± 0.24$^{a}$ | 4.65 ± 0.38$^{a}$ | 1.88 ± 0.77$^{a}$ |

Different letters in each column show significant differences ($p < 0.05$).

**Table 6**
Effect of 10-day storage at different temperatures on the color parameters of $NH_2$-MIL-53(Al)@PLA indicators exposed to 20 μM ammonia.

| Temperature(°C) | Color parameters | | | |
|---|---|---|---|---|
| | L* | a* | b* | ΔE |
| Freezer | 62.30 ± 0.77 | 0.28 ± 0.21 | 6.53 ± 0.60 | 4.02 ± 0.47 |
| Refrigerator | 62.46 ± 0.12 | 0.33 ± 0.11 | 6.59 ± 0.25 | 2.71 ± 0.26 |
| Ambient | 61.82 ± 1.56 | 0.50 ± 0.51 | 6.68 ± 0.67 | 3.81 ± 0.85 |

structure, which shielded the porous $NH_2$-MIL-53(Al)@PLA framework from environmental degradation. The marginal differences in ΔE values among different temperatures could stem from minor physical aging and chain relaxation of the PLA matrix, which can subtly modulate local gas diffusion pathways and free volume distribution without blocking the active sensing sites (Feng et al., 2026). This robust post-storage responsiveness is consistent with Hashemian et al. (2023), who demonstrated that cellulose acetate/HKUST-1 composites preserved stable and repeatable ammonia-sensing performance over multiple cycles due to the structural resilience of the embedded MOF interface.

### 3.2.12. *Migration studies and food safety assessment*

The aluminum ion migration from the $NH_2$-MIL-53(Al)@PLA indicator was strongly influenced by the chemical nature of the food simulants (Fig. 6). The lowest migration occurred in distilled water (<0.02 mg/kg), followed by 10% ethanol (<0.20 mg/kg), whereas higher release levels were detected in 3% acetic acid (1.6 mg/kg) and sunflower oil (3.9 mg/kg). These findings demonstrate that aluminum leaching is an environment-dependent process heavily dictated by the surrounding medium. The negligible aluminum release in distilled water reflects the exceptional hydrolytic stability of $NH_2$-MIL-53(Al), which originates from the strong Al–O coordination bonds between $Al^{3+}$ centers and the carboxylate groups of the linkers. According to the Hard-Soft Acid-Base (HSAB) theory, these interactions are thermodynamically robust, effectively preventing framework hydrolysis (Zhao et al., 2026). This minimal leaching aligns with the reduced moisture absorption discussed in Section 3.2.9 and corroborates the findings of Hu et al. (2015), who noted that aluminum- and zirconium-based frameworks exhibit superior resistance to hydrolytic degradation compared to zinc- or copper-based alternatives (Han et al., 2025). In 10% ethanol, the migration remained well below safety thresholds, indicating that low alcohol concentrations do not compromise the MOF's structural integrity. The minor increment relative to water is ascribed to slight matrix swelling and increased free volume within the PLA network, facilitating partial mass transfer rather than framework breakdown.

Conversely, the elevated aluminum migration in 3% acetic acid (1.6 mg/kg) is consistent with the aggressive nature of acidic media toward coordination networks. In accordance with EU testing guidelines, 3% acetic acid simulates acidic foods (pH < 4.5) and represents a worst-case scenario (Grob et al., 2009). This increased leaching is attributed to proton-induced competitive interactions that alter the metal–ligand coordination equilibria without necessarily causing complete structural collapse (McHugh et al., 2018). Crucially, this limited metal release did not alter the colorimetric parameters (ΔE) or color stability of the film across the investigated pH range, demonstrating that partial ion leaching and colorimetric response are decoupled phenomena.

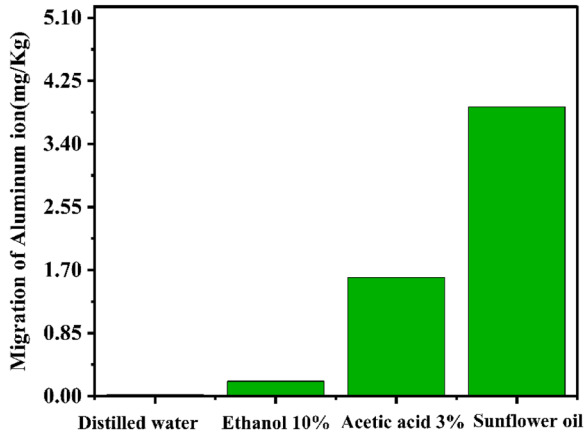


**Fig. 6.** Migration of aluminum ions from the $NH_2$-MIL-53(Al)@PLA indicator into different food simulants.

In sunflower oil, the migration reached 3.9 mg/kg, which is governed by an interfacial transport mechanism rather than chemical degradation. Due to the non-polar nature of the lipid simulant, aluminum release is initiated primarily at MOF particles located near the polymer–food interface, where weakly coordinated or defect-associated Al species detach and diffuse through local free-volume regions of the PLA matrix. This process is driven by the poor compatibility between the polar MOF surface and the hydrophobic oil phase, favoring surface desorption over bulk degradation.

Nevertheless, the aluminum levels detected in 3% acetic acid and sunflower oil slightly exceed the Specific Migration Limit (SML) of 1 mg/kg stipulated by Commission Regulation (EU) No 10/2011 (amended by EU 2020/1245) (EU, 2026). This indicates that while the developed indicator is highly stable and safe for aqueous and hydroalcoholic products (such as fresh fish or seafood with neutral/low-fat profiles), further matrix sealing or coating optimization is required prior to its commercial application in direct contact with highly acidic or oily foods.

## 3.3. *Application of the $NH_2$-MIL-53(Al)@PLA indicator for fish freshness evaluation*

In this study, a colorimetric indicator based on $NH_2$-MIL-53(Al)@PLA was developed and evaluated for its ability to monitor fish freshness during storage at room temperature (25 ± 1 °C) (TableS2, Supplementary Information) and under refrigeration (4 ± 1 °C) (Table S3, Supplementary Information).

Fish stored at room temperature spoiled within 60 h. At the initial stage (0 h), TVB-N was 7.24 ± 0.13 mg/100 g, pH was 6.05 ± 0.03, and TVC was 4.06 ± 0.08 log CFU/g. The $NH_2$-MIL-53(Al)@PLA indicator showed a creamy-white color with a low ΔE value (0.67 ± 0.01), indicating that the fish was fresh. After 24 h, the quality parameters increased to TVB-N of 16.24 ± 0.11 mg/100 g, pH of 6.42 ± 0.12, and TVC of 7.52 ± 0.10 log CFU/g. The indicator turned light yellow (ΔE = 6.26 ± 0.35), suggesting a transition to a semi-fresh state. At 42 h, the fish was identified as spoiled according to the criteria of TVB-N > 25 mg/100 g and TVC > 7 log CFU/g, and the indicator exhibited a yellow-brown color (ΔE = 14.51 ± 0.15). After 60 h, the sample was completely unfit for consumption as TVB-N exceeded 42.62 ± 0.11 mg/100 g and TVC surpassed 11.25 ± 0.11 log CFU/g. The $NH_2$-MIL-53(Al)@PLA indicator turned brown (ΔE = 22.45 ± 0.32), clearly indicating severe spoilage (Fig. 7a–c).

Under refrigerated conditions, the fish maintained acceptable freshness for a longer period of time, and the deterioration of quality progressed gradually over 11 days. On day 0, TVB-N was 7.13 ± 0.21 mg/100 g, pH was 6.15 ± 0.20, and TVC was 4.29 ± 0.26 log CFU/g, while the indicator exhibited a creamy-white color (ΔE = 0.34 ± 0.03). By day 5, a slight increase in spoilage indices was observed, with TVB-N of 19.32 ± 0.23 mg/100 g and TVC of 7.31 ± 0.02 log CFU/g, accompanied by a color change of the indicator to yellow (ΔE = 7.35 ± 0.13), indicating a semi-fresh stage. By day 9, a pronounced increase in spoilage indicators was observed, with pH, TVB-N, and TVC values reaching 7.25 ± 0.09, 35.54 ± 0.73 mg/100 g, and 11.57 ± 0.62 log CFU/g, respectively. Correspondingly, the indicator exhibited a distinct color transition from dark yellow to light brown. Finally, after 11 days, the indicator showed a dark brown color (ΔE = 21.19 ± 0.20), corresponding to advanced spoilage, with TVB-N > 40 mg/100 g, TVC > 11.80 log CFU/g, and pH > 7.31 (Fig. 8a-c).

These results closely align with the observations of Wang et al. (2024), who employed bimetallic zinc-copper Nano rods (ZnCu-BTC) as nanoscale additives in a potato starch/polyvinyl alcohol (PS/PVA) composite film. Their sensor demonstrated excellent colorimetric sensitivity toward ammonia, enabling real-time evaluation of shrimp freshness (Wang et al., 2024).

Figs. 7d-f and 8d-f illustrate the relationship between the color change of the $NH_2$- MIL -53(Al)@PLA indicator (based on the ΔE parameter) and the main quality indices of fish including pH, TVB N, and

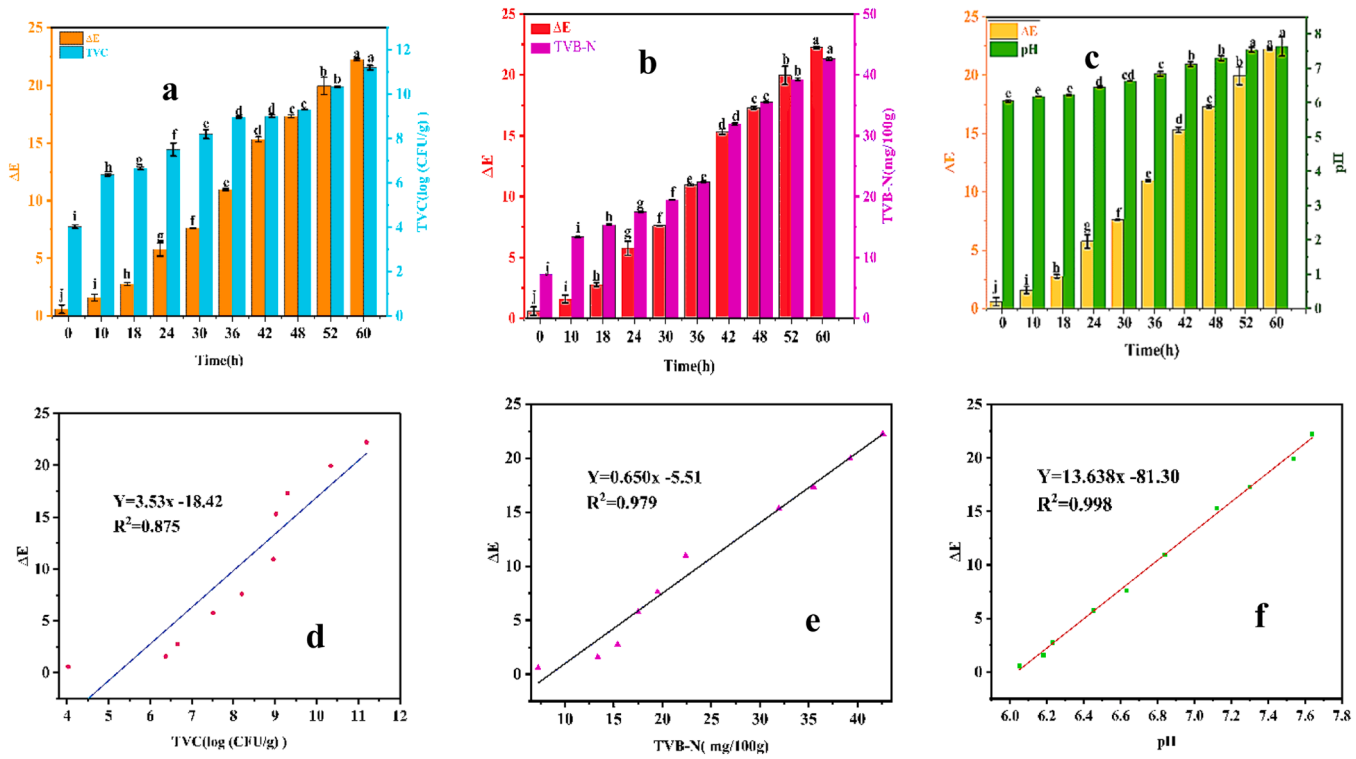


**Fig. 7.** Evaluation of color parameter changes of the of $NH_2$-MIL-53(Al)@PLA indicator and fish quality during storage at room temperatures (a, b, and c); Correlation between the ΔE of the indicator and the fish quality indices during storage (d, e, and f).

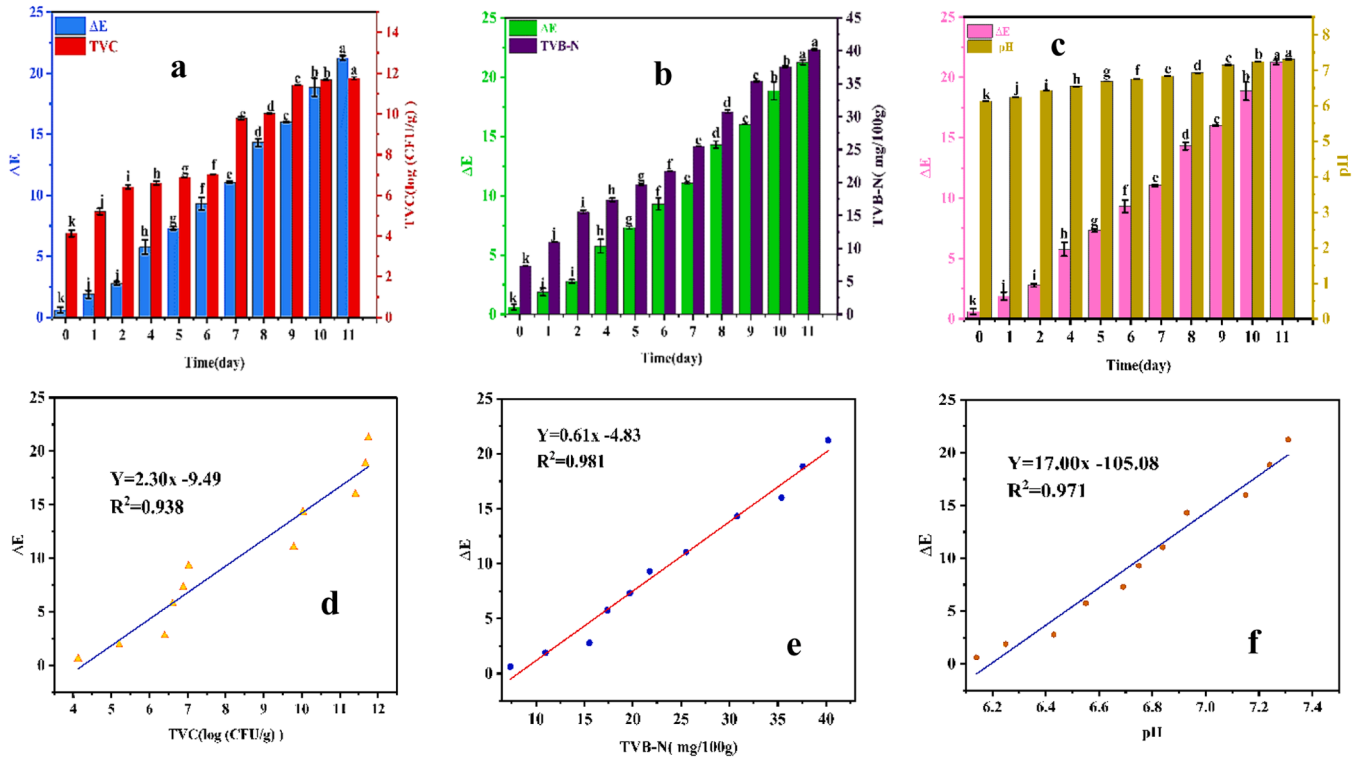


**Fig. 8.** Evaluation of color parameter changes of the of $NH_2$-MIL-53(Al)@PLA indicator and fish quality during storage at refrigerator temperatures (a, b, and c); Correlation between the ΔE of the indicator and the fish quality indices during storage (d, e, and f).

TVC during storage at two temperature conditions: room temperature (25 °C) and refrigerated temperature (4 °C), respectively. The results show that as storage time increases, the values of pH, TVB N, and TVC continuously rise, accompanied by a noticeable increase in the ΔE parameter of the colorimetric indicator. This concurrent upward trend demonstrates that the magnitude of the indicator's color change has a

direct and linear relationship with the extent of fish spoilage and can therefore serve as a reliable measure for assessing sample freshness.

Analysis of the regression equations and coefficients of determination ($R^2$) shows that the experimental data exhibit excellent linear fitting, with $R^2$ values ranging from 0.981 to 0.998. This demonstrates the stable performance, high optical stability, and chemical durability of the $NH_2$-MIL-53(Al)@PLA indicator making it suitable for long-term freshness evaluation of products under storage. Overall, the results show that the colorimetric parameter ΔE can be used as a quantitative and reliable indicator for estimating spoilage level and determining fish freshness. Therefore, it can be concluded that the $NH_2$-MIL-53(Al)@PLA colorimetric indicator has a high ability to detect variations caused by the production of volatile nitrogenous compounds and enables visual and non-destructive evaluation of fish spoilage and quality under both temperature conditions.

To provide a clear comparison of the spoilage progression under two storage temperatures, Fig. 9a–f were prepared illustrating three key stages: fresh, semi-fresh, and spoiled, along with the corresponding appearance of the fish and the color response of the $NH_2$-MIL-53(Al)@PLA indicator. At room temperature (25 °C), the fresh stage was observed at 0 h, with a firm texture and bright appearance, accompanied by a light-white indicator color. The semi-fresh stage appeared at 30 h, during which the fish showed slight changes in appearance and the indicator turned pale yellow. The spoiled stage was reached at 60 h, when visible spoilage of the fish occurred and the indicator changed to dark brown. Under refrigerated storage (4 °C), the same three stages occurred at later times: the fresh stage was observed on day 0 with a light-white indicator, the semi-fresh stage appeared on day 5 with a golden yellow indicator, and the completed spoiled stage was observed on day 11, accompanied by a dark brown indicator color. This three-stage comparative illustration provides a concise and visually intuitive representation of fish quality deterioration and the corresponding indicator color transitions under both temperature conditions.

### 3.4. Comparative performance analysis

To benchmark the analytical and practical efficiency of the $NH_2$-MIL-53(Al)@PLA indicator, its performance was compared with recently reported MOF-based freshness sensors (Table 7). Although several reported sensors achieve lower limits of detection (often in the ppb range), many of these platforms rely on multi-component sensing architectures, enzyme-assisted amplification, or unstable natural pigments (e.g., anthocyanins). In contrast, the present $NH_2$-MIL-53(Al)@PLA film operates via direct host–guest interactions between volatile amines and the inherent amino-functionalized framework, completely eliminating the need for auxiliary dyes or signal amplification agents. The target gas molecules migrate into the one-dimensional channels of $NH_2$-MIL-53(Al), inducing metal-center coordination and electronic perturbations that yield a distinct, macroscopically observable color transition from creamy white to dark brown. Unlike natural-dye-incorporated systems that suffer from pigment leaching and environmental degradation, our dye-free platform exhibits superior structural robustness and reduced susceptibility to premature degradation.

Furthermore, compared to fluorescence-based MOF sensors, the developed colorimetric indicator offers distinct operational advantages despite its higher LOD. While fluorescent platforms utilize sophisticated optical phenomena—such as aggregation-induced emission (AIE), excited-state intramolecular proton transfer (ESIPT), or Förster resonance energy transfer (FRET)—they demand specialized optical excitation sources, rare-earth metals, and benchtop spectrophotometers. This instrumentation dependence limits their real-time, cost-effective deployment in commercial smart packaging. Conversely, the $NH_2$-MIL-53(Al)@PLA film provides a simplified, label-free architecture that ensures direct naked-eye readability, excellent prolonged storage stability, and successful validation in real fish samples under both ambient and refrigerated conditions.

## 4. Conclusion

This study developed a highly responsive colorimetric indicator, $NH_2$-MIL-53(Al)@PLA, capable of rapidly, non-destructively, and reliably monitoring seafood freshness through distinct and irreversible naked-eye color changes induced by spoilage-related volatile amines. The indicator demonstrated strong analytical performance, exhibiting a low liquid-phase detection limit of 5.24 μM (corresponding to a conservative upper-bound gas-phase equivalent of 128.12 ppm) and clear linear correlations with key freshness indices, including matrix pH, TVB-N, and TVC. Structural analyses confirmed that the sensing mechanism

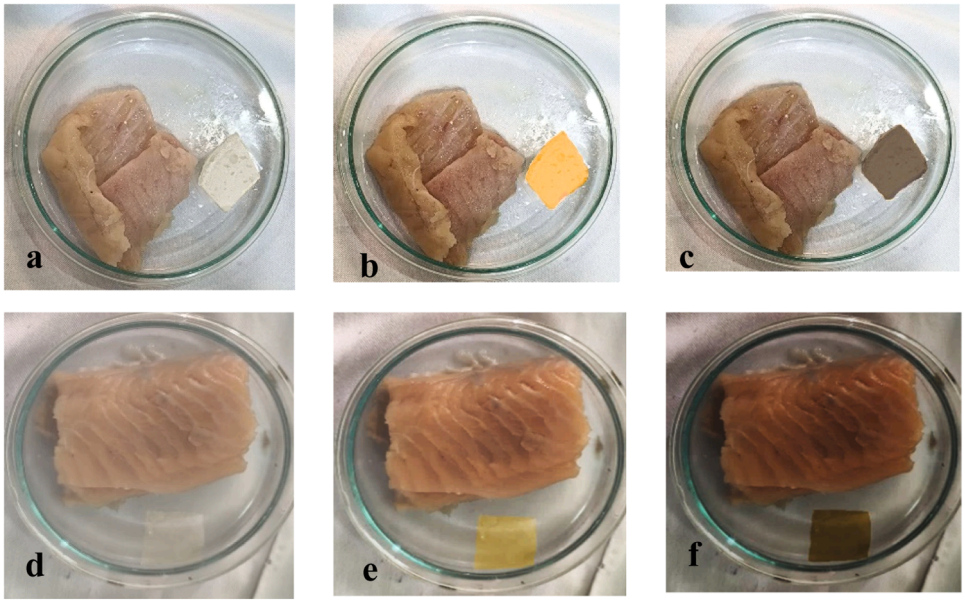


**Fig. 9.** Stages of fish spoilage under two storage conditions monitored using the $NH_2$-MIL-53(Al)@PLA indicator. At room temperature (25 °C), (a) represents the fresh stage at 0 h, (b) the semi-fresh stage at 30 h, and (c) the spoiled stage at 42 h. Under refrigerated storage (4 °C), (d) corresponds to the fresh stage at day 0, (e) to the semi-fresh stage at day 6, and (f) to the spoiled stage at day 11.

**Table 7**
Comparative analysis of recent MOF-based indicators for meat and seafood freshness monitoring.

| Indicator Component of | Detection Mode | Sensitivity (LOD)/ Response Time | Storage Stability | Real Sample Validation | Reference |
|---|---|---|---|---|---|
| MOF(HKUST-1) + Cellulose acetate | Colorimetric | 0.02 ppm | 4 days | Fish and chicken | (Hashemian et al., 2023) |
| Tragacanth hydrogel + MOF-5 + natural dyes | Fluorometric / Colorimetric | 49.6 ppb | 5 days | Fish and chicken, | (Hashemian et al., 2024) |
| PVA/corn starch+ UiO-66-$NH_2$-Zr/ Cu-MOF-$NH_2$ + roselle anthocyanin | Colorimetric | $\Delta E = 54.58$(30 min) for UiO-66-$NH_2$–Zr $\Delta E = 56.74$ (10 min) for Cu-MOF-$NH_2$ | $\Delta E < 2.5$ after 15 days storage (4 °C and 25 °C, 50% RH) | pork and shrimp | (Huang et al., 2025) |
| Gelatin nanofiber+ red cabbage extract (anthocyanins) + ZIF-8 | Colorimetric | $\Delta E \geq 5$ within 10 min | 28 days (refrigerated) | fish | (Najafi & Kahyaoglu, 2026) |
| Dye@UiO-66-Br+Chitosan | Colorimetric array + deep learning | LOD = 37.17 ppm (equilibrium: 420 s | High RGB precision at 40 ppm | Shrimp | (Ma et al., 2021) |
| BTCP-Ac dye + Eu-MOF + bacterial cellulose | Fluorescent / colorimetric | LOD = 0.68 ppm | 30 days (No signal decay) | Chicken | (Ma et al., 2025) |
| $NH_2$-MIL-53(Al) + PLA | Colorimetric | LOD = 128.12 ppm (5.24 μM) | $\Delta E \leq 2.33$ after 10 days (−18, 4, 25 °C, 75% RH) | Fish (Spoilage tracking) | This work |

arises from target-specific interactions between nitrogenous volatiles and the MOF framework, accompanied by framework breathing and partial pore blockage. Post-exposure XRD analysis revealed reversible diffraction peak shifts, confirming guest-induced lattice flexibility while preserving the long-range crystalline architecture of $NH_2$-MIL-53(Al). In addition to its sensing function, the composite film exhibited meaningful antibacterial activity against both *E. coli* (21.20 ± 0.10 mm zone of inhibition) and *Staphylococcus aureus* (30.34 ± 0.22 mm zone of inhibition), enhancing its potential role as a semi-active smart packaging component. The PLA matrix effectively supported uniform MOF distribution under high-shear casting, ensuring consistent colorimetric behavior. Furthermore, the indicator displayed reduced moisture absorption (~2.5% lower than neat PLA), excellent thermal stability (with the MOF remaining intact up to ~450 °C), and robust chromatic stability under frozen, refrigerated, and ambient storage conditions for up to 10 days. Importantly, ICP-OES migration studies demonstrated negligible aluminum release in water (<0.02 mg $kg^{-1}$) and 10% ethanol (<0.20 mg $kg^{-1}$), remaining strictly below international specific migration limits (SML) and validating its toxicological safety for food-contact applications. Practical trials utilizing trout fillets confirmed the indicator's capacity to accurately track real-time spoilage progression under diverse temperature profiles. Overall, $NH_2$-MIL-53(Al)@PLA represents a robust, environmentally compatible, and promising platform for intelligent seafood freshness monitoring. Future investigations should focus on scaling up the production of these indicators and evaluating their mechanical and functional performance under commercial protective atmosphere packaging conditions.

## Ethical statement - studies in humans and animals

This study does not involve human or animal subjects.

## CRediT authorship contribution statement

**Razieh Mansouri Habibabadi:** Writing – original draft, Methodology, Investigation. **Kazem Karami:** Software, Resources, Project administration, Conceptualization. **Zahra Teymouri:** Writing – review & editing, Investigation, Formal analysis. **Hajar Shekarchizadeh:** Software, Methodology, Conceptualization.

## Declaration of competing interest

The authors declare that they have no known competing financial interests or personal relationships that could have appeared to influence the work reported in this paper.

## Supplementary materials

Supplementary material associated with this article can be found, in the online version, at doi:10.1016/j.afres.2026.102480.

## Data availability

No data was used for the research described in the article.

## References


Abid, M., Mallet, B., Lamnawar, K., & Maazouz, A. (2018). Crystallization of poly(lactic acid) (PLA): Effect of nucleating agents and structure–properties relationships. *Journal of Composites and Biodegradable Polymers, 6*, 34–46. https://doi.org/10.12974/2311-8717.2018.06.5

Ahmed, M., Saini, P., Iqbal, U., & Sahu, K. (2024). Edible microbial cellulose-based antimicrobial coatings and films containing clove extract. *Food Production, Processing and Nutrition, 6*(1), 65. https://doi.org/10.1186/s43014-024-00241-9

Akbari, S. M., & Nikoo, A. M. (2025). Fabrication of pH-sensitive smart indicator film from polylactic acid and elderberry anthocyanin for monitoring chicken spoilage. *Packaging Technology and Science, 38*, 640–659. https://doi.org/10.1002/pts.2897

Al-Qahtani, S. D., Al-Senani, G. M., Bukhari, A. A. H., Al-Anazi, M., Parveen, H., Faridi, U., & El-Afify, M. A. M. (2026). Covalent engineering of a phenanthroline-modified NH2-MIL-53(Al) MOF for the dual-mode sensing of As3+ and Fe2+ in complex environmental and dietary matrices. *RSC Adv, 16*, 27718–27737. https://doi.org/10.1039/d6ra02963a

Amaregouda, Y., Kamanna, K., & Gasti, T. (2022). Fabrication of intelligent/active films based on chitosan/polyvinyl alcohol matrices containing Jacaranda cuspidifolia anthocyanin for real-time monitoring of fish freshness. *International Journal of Biological Macromolecules, 218*, 799–815. https://doi.org/10.1016/j.ijbiomac.2022.07.174

Arshadi Edlo, A., & Akhbari, K. (2024). Modulated antibacterial activity in ZnO@ MIL-53 (Fe) and CuO@ MIL-53 (Fe) nanocomposites prepared by simple thermal treatment process. *Applied Organometallic Chemistry, 38*(2), Article e7326. https://doi.org/10.1002/aoc.7326

Boulé, R., Roland, C., Le Pollès, L., Audebrand, N., & Ghoufi, A. (2018). Thermal and guest-assisted structural transition in the $NH_2$-MIL-53(Al) metal–organic framework: A molecular dynamics simulation investigation. *Nanomaterials, 8*(7), 531. https://doi.org/10.3390/nano8070531

Cheng, X., Zhang, A., Hou, K., Liu, M., Wang, Y., Song, C., Zhang, G., & Guo, X. (2013). Size- and morphology-controlled NH2-MIL-53 (Al) prepared in DMF–water mixed solvents. *Dalton Transactions (Cambridge, England : 2003), 42*(37), Article 13698. https://doi.org/10.1039/C3DT51322J

Cheng, J.-H., Sun, D.-W., & Wei, Q. (2017). Enhancing visible and near-infrared hyperspectral imaging prediction of TVB-N level for fish fillet freshness evaluation by filtering optimal variables. *Food Analytical Methods, 10*(6), 1888–1898. https://doi.org/10.1007/s12161-016-0742-9

Commission Regulation (EU). (2026). No 10/2011 of 14 January 2011 on plastic materials and articles intended to come into contact with food (text with EEA relevance. Eur-Lex consolidated text 02011R0010 https://eur-lex.europa.eu/legal-content/EN/TXT/?uri=CELEX%3A02011R0010-20260223.

Couck, S., Denayer, J. F., Baron, G. V., Rémy, T., Gascon, J., & Kapteijn, F. (2009). An amine-functionalized MIL-53 metal−organic framework with large separation power for CO2 and CH4. *Journal of the American Chemical Society, 131*(18), 6326–6327. https://doi.org/10.1021/ja900555r

Dai, X., Cao, Y., Shi, X., & Wang, X. (2016). Non-isothermal crystallization kinetics, thermal degradation behavior and mechanical properties of poly(lactic acid)/MOF

composites prepared by melt-blending methods. *RSC Advances, 6*(75), 71461–71471. https://doi.org/10.1039/C6RA14190K

Dong, Y., Tian, X., & Zahid, M. (2025). Ligand removal in Ti-MOFs: Unlocking the potential of Pt nanoparticles for the selective hydrogenation of furfural. *The International Journal of Hydrogen Energy, 179*, Article 151700. https://doi.org/10.1016/j.ijhydene.2025.151700

Dorosti, F., & Alizadehdakhel, A. (2018). Fabrication and investigation of PEBAX/Fe-BTC, a high permeable and CO2 selective mixed matrix membrane. *Chemical Engineering Research and Design, 136*, 119–128. https://doi.org/10.1016/j.cherd.2018.01.029

Feng, S., Li, P., Yu, J., Peng, X., Gao, X., Tang, L., & Yu, X. (2026). Development of a highly sensitive and stable ammonia-responsive smart film using CoNi-MOF: Preparation, characterization, and application for graded shrimp freshness monitoring. *Food Research International (Ottawa, Ont), 238*, Article 119463. https://doi.org/10.1016/j.foodres.2026.119463

Gecgel, C., Gonca, S., Turabik, M., & Özdemir, S. (2022). An aluminum-based MOF and its amine form as novel biological active materials for antioxidant, DNA cleavage, antimicrobial, and biofilm inhibition activities. *Materials Today Sustainability, 19*, Article 100204. https://doi.org/10.1016/j.mtsust.2022.100204

Ghaly, A. E., Dave, D., Budge, S., & Brooks, M. S. (2010). Fish spoilage mechanisms and preservation techniques. *American Journal of Applied Sciences, 7*, 859–877. https://doi.org/10.3844/AJASSP.2010.859.877

Ghorbani, M., Divsalar, E., Molaei, R., Ezati, P., Moradi, M., Tajik, H., & Abbaszadeh, M. (2021). A halochromic indicator based on polylactic acid and anthocyanins for visual freshness monitoring of minced meat, chicken fillet, shrimp, and fish roe. *Innovative Food Science and Emerging Technologies, 74*, Article 102864. https://doi.org/10.1016/j.ifset.2021.102864

Gram, L., Ravn, L., Rasch, M., Bruhn, J. B., Christensen, A. B., & Givskov, M. (2002). Food spoilage—Interactions between food spoilage bacteria. *International Journal of Food Microbiology, 78*(1–2), 79–97. https://doi.org/10.1016/S0168-1605(02)00233-7

Grob, K., Stocker, J., & Colwell, R. (2009). Assurance of compliance within the production chain of food contact materials by good manufacturing practice and documentation–Part 2: Implementation by the compliance box; call for guidelines. *Food Control, 20*(5), 483–490. https://doi.org/10.1016/j.foodcont.2008.07.018

Habibabadi, R. M., Karami, K., Jamshidian, N., & Allafchian, A. (2026). Facile synthesis of $NH_2$-MIL-53(Al) decorated on COOH-modified $MoS_2$ nanosheets as high-performance supercapacitor electrode. *The Journal of Physics and Chemistry of Solids, 217*, Article 113854. https://doi.org/10.1016/j.jpcs.2026.113854

Han, Z., Yang, Y., Rushlow, J., Huo, J., Liu, Z., Hsu, Y. C., & Zhou, H. C. (2025). Development of the design and synthesis of metal–organic frameworks (MOFs)—From large scale attempts, functional oriented modifications, to artificial intelligence (AI) predictions. *Chemical Society Reviews, 54*(1), 367–395. https://doi.org/10.1039/D4CS00432A

Hashemian, H., Ghaedi, M., Dashtian, K., Mosleh, S., Hajati, S., Razmjoue, D., & Khan, S. (2023). Cellulose acetate/MOF film-based colorimetric ammonia sensor for non-destructive remote monitoring of meat product spoilage. *International Journal of Biological Macromolecules, 249*, Article 126065. https://doi.org/10.1016/j.ijbiomac.2023.126065

Hashemian, H., Ghaedi, M., Dashtian, K., Khan, S., Mosleh, S., Hajati, S., & Razmjoue, D. (2024). Highly sensitive fluorometric ammonia detection utilizing *Solenostemon scutellarioides* (L.) extracts in MOF-tragacanth gum hydrogel for meat spoilage monitoring. *Sensors & Actuators, B: Chemical, 406*, Article 135354. https://doi.org/10.1016/j.snb.2024.135354

Hsieh, Y. T., Nozaki, S., Kido, M., Kamitani, K., Kojio, K., & Takahara, A. (2020). Crystal polymorphism of polylactide and its composites by X-ray diffraction study. *Polymer Journal, 52*(7), 755–763. https://doi.org/10.1038/s41428-020-0343-8

Hu, Z., Khurana, M., Seah, Y. H., Zhang, M., Guo, Z., & Zhao, D. (2015). Ionized Zr-MOFs for highly efficient post-combustion $CO_2$ capture. *Chemical Engineering Science, 124*, 61–69. https://doi.org/10.1016/j.ces.2014.09.032

Huang, L., Yang, Z., Li, X., Hou, L., Alhassan, S. I., & Wang, H. (2021). Synthesis of hierarchical hollow MIL-53(Al)-$NH_2$ as an adsorbent for removing fluoride: Experimental and theoretical perspective. *Environmental Science and Pollution Research, 28*(6), 6886–6897. https://doi.org/10.1007/s11356-020-10975-x

Huang, K., Wang, L., Deng, Y., Zheng, H., Wu, S., Li, Z., Lei, H., Yu, Q., & Guo, Z. (2024). Development of amine-sensitive intelligent film with MIL-100 (Fe) as function filler based on anthocyanins/pectin for monitoring chilled meat freshness. *International Journal of Biological Macromolecules, 270*, Article 132463. https://doi.org/10.1016/j.ijbiomac.2024.132463

Huang, X., Zhang, K., Zhang, J., Zhai, X., Shi, J., Zou, X., & Li, Z. (2025). Polyvinyl alcohol/corn starch-based indicator films integrated with roselle anthocyanins into five metal-organic frameworks for monitoring chilled pork and shrimp freshness. *Innovative Food Science and Emerging Technologies, 105*, Article 104230. https://doi.org/10.1016/j.ifset.2025.104230

Jiang, F. Q., Zhang, R., Ba, D., Dong, W. W., Zhao, J., & Li, D. S. (2025). Enhanced proton conductivity in proton exchange membranes via integration of protic ionic liquid–encapsulated $NH_2$-MIL-53(Al) with sulfonated poly(ether ether ketone). *Zeitschrift für Anorganische und Allgemeine Chemie, 651*(9), Article e202500038. https://doi.org/10.1002/zaac.202500038

Kang, Y., Zhao, D., Cai, D., Jia, B., Fu, J., Li, X., Hu, J., & Li, L. (2024). Novel copper-based metal–organic skeleton smart tags that respond to ammonia for real-time visual freshness monitoring of shrimp. *Chemical Engineering Journal, 495*, Article 153388. https://doi.org/10.1016/j.cej.2024.153388

Kathuria, A., Brouwers, N., Buntinx, M., Harding, T., & Auras, R. (2018). Effect of MIL-53 (Al) MOF particles on the chain mobility and crystallization of poly(L-lactic acid). *Journal of Applied Polymer Science, 135*(3), Article 45690. https://doi.org/10.1002/app.45690

Khezerlou, A., Tavassoli, M., Alizadeh-Sani, M., Hashemi, M., Ehsani, A., & Bangar, S. P. (2023). Multifunctional food packaging materials: Lactoferrin loaded Cr-MOF in films-based gelatin/κ-carrageenan for food packaging applications. *International Journal of Biological Macromolecules, 251*, Article 126334. https://doi.org/10.1016/j.ijbiomac.2023.126334

Lentz, T. J., Seaton, M., Rane, P., Gilbert, S. J., McKernan, L. T., & Whittaker, C. (2019). *Technical report: The NIOSH occupational exposure banding process for chemical risk management*. NIOSH Publication 2019-132. https://doi.org/10.26616/NIOSHPUB2019132

Li, N., Qin, H., Tang, Q., Peng, D., Luo, X., Li, H., & Zou, Z. (2024). Development and application of intelligent packaging films based on carboxymethyl starch/PVA with Cu-LTE nanocrystal as functional compatibilizer. *Food Packaging and Shelf Life, 43*, Article 101306. https://doi.org/10.1016/j.fpsl.2024.101306

Li, M., Zeng, G., You, H., Xi, D., Huang, H., Kou, X., Farid, A., & Zhao, Y. (2025). Band-engineered α-$Fe_2O_3$@NiO p–n heterojunction for room-temperature $NH_3$ detection and real-time meat spoilage monitoring. *Nanomaterials, 15*(13), 1098. https://doi.org/10.3390/nano1513098

Loiseau, T., Serre, C., Huguenard, C., Fink, G., Taulelle, F., Henry, M., Bataille, T., & Férey, G. (2004). A rationale for the large breathing of the porous aluminum terephthalate (MIL-53) upon hydration. *Chemistry – A European Journal, 10*(6), 1373–1382. https://doi.org/10.1002/chem.200305413

Ma, P., Zhang, Z., Xu, W., Teng, Z., Luo, Y., Gong, C., & Wang, Q. (2021). Integrated portable shrimp-freshness prediction platform based on ice-templated metal–organic framework colorimetric combinatorics and deep convolutional neural networks. *ACS Sustainable Chemistry & Engineering, 9*(50), 16926–16936. https://doi.org/10.1021/acssuschemeng.1c04704

Ma, Y., Li, Y., Huang, T., Yang, X., Huang, J., & Huang, M. (2025). Preparation of an ammonia-responsive sensor based on bacterial cellulose film with enhanced AIE/ESIPT emission of fluorescent molecules bound to europium-based metal–organic framework. *Chemical Engineering Journal, 513*, Article 163034. https://doi.org/10.1016/j.cej.2025.163034

Mason, D. J., Power, E. G., Talsania, H., Phillips, I., & Gant, V. A. (1995). Antibacterial action of ciprofloxacin. *Antimicrobial Agents and Chemotherapy, 39*(12), 2752–2758. https://doi.org/10.1128/aac.39.12.2752

McHugh, L. N., McPherson, M. J., McCormick, L. J., Morris, S. A., Wheatley, P. S., Teat, S. J., McKay, D., Dawson, D. M., Sansome, C. E. F., Ashbrook, S. E., Stone, C. A., Smith, M. W., & Morris, R. E. (2018). Hydrolytic stability in hemilabile metal–organic frameworks. *Nature Chemistry, 10*, 415–423. https://doi.org/10.1038/s41557-018-0104

Mihaylov, M., Chakarova, K., Andonova, S., Drenchev, N., Ivanova, E., Sabetghadam, A., Seoane, B., Gascon, J., Kapteijn, F., & Hadjiivanov, K. (2016). Adsorption forms of CO2 on MIL-53 (Al) and NH2-MIL-53 (Al) as revealed by FTIR spectroscopy. *The Journal of Physical Chemistry C, 120*(41), 23584–23595. https://doi.org/10.1021/acs.jpcc.6b07492

Mohammadalinejhad, S., Almasi, H., & Moradi, M. (2020). Immobilization of echium amoenum anthocyanins into bacterial cellulose film: A novel colorimetric pH indicator for freshness/spoilage monitoring of shrimp. *Food Control, 113*, Article 107169. https://doi.org/10.1016/j.foodcont.2020.107169

Najafi, Z., & Kahyaoglu, L. N. (2026). Centrifugally spun gelatin nanofibers incorporated with red cabbage extract and ZIF-8 for colorimetric monitoring of fish freshness. *Food Chemistry, 508*, Article 148470. https://doi.org/10.1016/j.foodchem.2026.148470

Noorani, N., & Mehrdad, A. (2023). Impregnation of amine functionalized deep eutectic solvents in $NH_2$-MIL-53(Al) MOF for $CO_2/N_2$ separation. *Scientific Reports, 13*(1), Article 13012. https://doi.org/10.1038/s41598-023-40191-9

Poddar, D., Goel, G., & Pattanayek, S. K. (2025). Based biopolymer seafood packaging with integrated colorimetric ammonia detection for intelligent barrier technologies. *Langmuir : The ACS Journal of Surfaces and Colloids, 495*(32), Article 153388. https://doi.org/10.1016/j.cej.2024.153388

Prakash, G., Pandey, D., Maurya, S., & Pandey, V. (2025). Smart and sustainable: Review of AI-driven approaches in biodegradable food packaging systems. *European Journal of Nutrition & Food Safety, 17*(8), 235–244. https://doi.org/10.9734/ejnfs/2025/v17i81815

Quiros, J., Boltes, K., Aguado, S., de Villoria, R. G., Vilatela, J. J., & Rosal, R. (2015). Antimicrobial metal–organic frameworks incorporated into electrospun fibers. *Chemical Engineering Journal, 262*, 189–197. https://doi.org/10.1016/j.cej.2014.09.104

Rahimpoor, R., Firoozichahak, A., Alizadeh, S., Serkan, H., & Nematollahi, D. (2022). Application of MIL-53 (Al)-NH2 as a dispersive microsolid-phase extraction material for determination of cyclophosphamide in urine by high-performance liquid chromatography. *ACS Omega, 7*(41), 36643–36652. https://doi.org/10.1021/acsomega.2c04660

Razavi-Tehrani, S., & Shekarchizadeh, H. (2026). Development of self-healing gelatin films based on polyethyleneimine with $SiO_2$ nanoparticles as functional fillers for active/smart food packaging. *Future Foods, 13*, Article 100968. https://doi.org/10.1016/j.fufo.2026.100968

Segura González, E. A., Olmos, D., Lorente, M.Á., Vélaz, I., & González-Benito, J. (2018). Preparation and characterization of polymer composite materials based on PLA/$TiO_2$ for antibacterial packaging. *Polymers, 10*(12), 1365. https://doi.org/10.3390/polym10121365

Serra-Crespo, P., Gobechiya, E., Ramos-Fernandez, E. V., Juan-Alcañiz, J., Martinez-Joaristi, A., Stavitski, E., Kirschhock, C. E., Martens, J. A., Kapteijn, F., & Gascon, J. (2012). Interplay of metal node and amine functionality in NH2-MIL-53: Modulating breathing behavior through intra-framework interactions. *Langmuir : The ACS*

*Journal of Surfaces and colloids, 28*(35), 12916–12922. https://doi.org/10.1021/la302824j

Singh, V. M., Koo, D., Palmese, G. R., & Cairncross, R. A. (2011). Synthesis of polylactide with varying molecular weight and aliphatic content: Effect on moisture sorption. *Journal of Applied Polymer Science, 120*(5), 2543–2549. https://doi.org/10.1002/app.33271

Sompornpailin, D., Mongconpattarasuk, P., Ratanatawanate, C., Apiratikul, R., Chu, K. H., & Punyapalakul, P. (2022). Adsorption of nonsteroidal anti-inflammatory drugs onto composite beads of a 1D flexible framework MIL-53 (Al): Adsorption mechanisms and fixed-bed study. *Journal of Environmental Chemical Engineering, 10*(4), Article 108144. https://doi.org/10.1016/j.jece.2022.108144

Sorribas, S., Zornoza, B., Serra-Crespo, P., Gascon, J., Kapteijn, F., Téllez, C., & Coronas, J. (2016). Synthesis and gas adsorption properties of mesoporous silica-NH2-MIL-53 (Al) core–shell spheres. *Microporous and Mesoporous Materials : The Official Journal of the International Zeolite Association, 225*, 116–121. https://doi.org/10.1016/j.micromeso.2015.12.004

Teymouri, Z., Shekarchizadeh, H., & Karami, K. (2025). Innovative intelligent packaging using a CuMOF immobilized on cellulose matrix: A dual-mode sensing platform for fish spoilage detection. *Applied Food Research, 5*, Article 100953. https://doi.org/10.1016/j.afres.2025.100953

Van Tran, T., Jalil, A. A., Nguyen, D. T. C., Alhassan, M., Nabgan, W., Cao, A. N. T., Nguyen, T. M., & Vo, D.-V. N. (2023). A critical review on the synthesis of NH2-MIL-53 (Al) based materials for detection and removal of hazardous pollutants. *Environmental Research, 216*, Article 114422. https://doi.org/10.1016/j.envres.2022.114422

Wang, M., Nian, L., Wu, J., Cheng, S., Yang, Z., & Cao, C. (2023). Visible light-responsive chitosan/sodium alginate/QDs@ZIF-8 nanocomposite films with antibacterial and ethylene scavenging performance for kiwifruit preservation. *Food Hydrocolloids, 145*, Article 109073. https://doi.org/10.1016/j.foodhyd.2023.109073

Wang, P., Qin, H., He, D., Zou, Z., Xu, L., & Tang, Q. (2024). Developing colorimetric ammonia-sensing nanocomposite films based on potato starch/PVA and ZnCu-BTC nanorods for real-time monitoring food freshness. *International Journal of Biological Macromolecules, 277*, Article 134376. https://doi.org/10.1016/j.ijbiomac.2024.134376

Xia, L., Wang, P., Zheng, S., Zheng, T., Huang, B., Li, H., & Tang, Q. (2025). Development of sustainable active smart Fe-CIT/PVA nanocomposite-based films for monitoring shrimp freshness. *Food Chemistry, 495*, Article 146404. https://doi.org/10.1016/j.foodchem.2025.146404

Xu, Z., Cheng, Z., Tang, Q., Huang, K., Li, H., & Zou, Z. (2023). Ammonia-sensitive cellulose acetate-based films incorporated with Co-BIT microcrystals for smart packaging application. *Carbohydrate Polymers, 316*, Article 121045. https://doi.org/10.1016/j.carbpol.2023.121045

Xu, X., Huang, K., He, D., Huang, B., Tang, Q., Li, H., & Zou, Z. (2025). Biocompatible starch based smart active packaging film engineered with a novel CuNa-MOF colorimetric ammonia sensing agent based on crystal-to-crystal transformation. *Food Packag. Shelf Life, 49*, Article 101498. https://doi.org/10.1016/j.fpsl.2025.101498

Zahid, M., Jassim, G. S., Jawad, H. A. M., Khan, M. F., & Ismail, A. (2023). Selective hydrogenation of detrimental 4-nitrophenol to desired 4-aminophenol over potent PtCo intermetallic nanoparticles entrapped within the pores of Cr-BDC MOFs. *Inorganic Chemistry Communications, 150*, Article 110549. https://doi.org/10.1016/j.inoche.2023.110549

Zahid, M., Ismail, A., Ullah, R., Ali, U., Raziq, F., Alrebdi, T. A., & Qiao, L. (2024). Pt–N catalytic centres concisely enhance interfacial charge transfer in amines functionalized Pt@MOFs for selective conversion of $CO_2$ to $CH_4$. *Journal of Colloid and Interface Science, 672*, 370–382. https://doi.org/10.1016/j.jcis.2024.05.186

Zgurskaya, H. I., López, C. A., & Gnanakaran, S. (2015). Permeability barrier of gram-negative cell envelopes and approaches to bypass it. *ACS Infectious Diseases, 1*(11), 512–522. https://doi.org/10.1021/acsinfecdis.5b00097

Zhai, X., Li, Z., Shi, J., Huang, X., Sun, Z., Zhang, D., Zou, X., Sun, Y., Zhang, J., & Holmes, M. (2019). A colorimetric hydrogen sulfide sensor based on gellan gum-silver nanoparticles bionanocomposite for monitoring of meat spoilage in intelligent packaging. *Food Chemistry, 290*, 135–143. https://doi.org/10.1016/j.foodchem.2019.03.138

Zhang, Q.-C., Xia, G.-P., Liang, J.-Y., Zhang, X.-L., Jiang, L., Zheng, Y.-G., & Wang, X.-Y. (2020). NH2-MIL-53 (Al) polymer monolithic column for in-tube solid-phase microextraction combined with UHPLC-MS/MS for detection of trace sulfonamides in food samples. *Molecules (Basel, Switzerland), 25*(4), 897. https://doi.org/10.3390/molecules25040897

Zhang, J., Zhang, X., Huang, X., Shi, J., Sobhy, R., Khalifa, I., & Zou, X. (2024). Ammonia-responsive colorimetric film of phytochemical formulation (alizarin) grafted onto ZIF-8 carrier with poly(vinyl alcohol) and sodium alginate for beef freshness monitoring. *Journal of Agricultural and Food Chemistry, 72*(20), 11706–11715. https://doi.org/10.1021/acs.jafc.4c02227

Zhao, K., Shuaibu, A., Fu, Z., Xie, J., & Ding, Z. (2026). A critical review of the toxicity, safety, and regulatory landscape of metal-organic frameworks in food packaging. *Coordination Chemistry Reviews, 556*, Article 217689. https://doi.org/10.1016/j.ccr.2026.217689